Julius-Maximilians-Universität Würzburg


# SINGLE-MOLECULE DYNAMICS AT A BOTTLENECK: A SYSTEMATIC STUDY OF THE NARROW ESCAPE PROBLEM IN A DISC

Einzelmoleküldynamik an einem Engpass: Eine systematische Untersuchung des Narrow Escape Problems in einer Scheibe

**Doctoral thesis**

for a doctoral degree at the Graduate School of Life Sciences

Section: Integrative Biology

submitted by

**Elisabeth Meiser**

born in Worms

Würzburg, 2023

This document is licensed under the Creative Commons Attribution-ShareAlike 4.0 International License (CC BY-SA 4.0):
http://creativecommons.org/licenses/by-sa/4.0 This CC license does not apply to third party material (attributed to another source) in this publication.

submitted on: _____

## Members of the Thesis Committee

Chairperson:

**Prof. Dr. Christian Janzen**

Department for Cell and Developmental Biology

Julius-Maximilians-Universität Würzburg

Primary supervisor and first examiner:

**Dr. Susanne Fenz**

Department for Cell and Developmental Biology

Julius-Maximilians-Universität Würzburg

Supervisor:

**Prof. Dr. Markus Engstler**

Department for Cell and Developmental Biology

Julius-Maximilians-Universität Würzburg

Supervisor and second examiner:

**Prof. Dr. Markus Sauer**

Department for Biotechnology

Julius-Maximilians-Universität Würzburg

Supervisor:

**Prof. Dr. Christian Stigloher**

Imaging Core Facility

Julius-Maximilians-Universität Würzburg

# Affidavit

I hereby confirm that my thesis entitled 'Single- molecule dynamics at a bottleneck: a systematic study of the narrow escape problem in a disc' is the result of my own work. I did not receive any help or support from commercial consultants. All sources and/or material applied are listed and specified in the thesis. Furthermore, I confirm that this thesis has not yet been submitted as part of another examination process neither in identical nor in similar form.

Date: _____ Signature: _____

# Eidesstattliche Erklärung

Ich erkläre hiermit an Eides statt, dass ich die vorliegende Dissertation "Einzelmoleküldynamik an einem Engpass: eine systematische Untersuchung des Narrow Escape Problems in einer Scheibe" eigenständig, d.h. insbesondere ohne die Hilfe oder Unterstützung von kommerziellen Promotionsberatern, angefertigt habe. Ergänzend bestätige ich, dass ich keine anderen als die von mir angegebenen Quellen oder Hilfsmittel verwendet habe. Ich erkläre außerdem, dass diese Dissertation weder in gleicher noch in ähnlicher Form bereits in einem Prüfungsverfahren vorgelegen hat.

Date: _____ Signature: _____

# Abstract

Diffusion facilitates numerous reactions within the biological context of a cell. It is remarkable how the cost-efficient random process of Brownian motion promotes fast reactions. From the narrow escape theory, it is possible to determine the mean first passage time of such processes based on their reaction space and diffusion coefficient. The narrow escape theory of Brownian particles is characterized by a confining domain with reflective boundaries and a small reaction site. In this thesis, the mean first passage time was systematically tested in a disc as a function of the escape opening size *in vitro* and *in silico*. For the *in vitro* experiments, a model system of patterned supported-lipid bilayers (SLB) was established. Such a model is prepared by a combined colloid metalization approach, where a gold scaffold on glass facilitates assembly of SLB patches of distinct sizes through vesicle fusion. The model setup was evaluated and found to match all necessary requirements to test the narrow escape problem *in vitro*. In particular, the reflectivity of the boundaries, the unhindered, free diffusion of the tracer lipids, and the distinct area were assessed. Observed results of the mean first passage time agreed with the theory of the narrow escape problem. There was excellent agreement in both absolute values and across a range of small escape opening sizes. Additionally, I developed a straightforward method, a correction factor, to calculate the mean first passage time from incomplete experimental traces. By re-scaling the mean first passage time to the fraction of particles that escaped, I was able to overcome the lifetime limitations of fluorescent probes. Previously inaccessible measurements of the mean first passage time relying on fluorescent probes will be made possible through this approach. The *in vitro* experiments were complemented with various *in silico* experiments. The latter were based on random walk simulations in discs, mimicking the *in vitro* situation with its uncertainties. The lifetime of single particles was either set sufficiently long to allow all particles to escape, or was adjusted to meet the lifetime limitations observed in the *in vitro* experiments. A comparison of the mean first passage time from lifetime-unlimited particles to the corrected, lifetime-limited particles did support the use of the correction factor. In agreement with the narrow escape theory, it was experimentally found that the mean first passage time is independent of the start point of the particle within the domain. This is when the particle adheres to a

minimum distance to the escape site. In general, the presented random walk simulations do accurately represent the *in vitro* experiments in this study. The required hardware for the establishment of an astigmatism-based 3D system was installed in the existing microscope. The first attempts to analyze the obtained 3D imaging data gave insight into the potential of the method to investigate molecule dynamics in living trypanosome cells. The full functionality will be realized with the ongoing improvement of image analysis outside of this thesis.

Part of the results and methods of this dissertation was submitted for publication entitled 'Experiments in micro-patterned model membranes support the narrow escape theory'.

# Zusammenfassung

Diffusion erleichtert zahlreiche Reaktionen im biologischen Kontext einer Zelle. Es ist bemerkenswert, wie der kosteneffiziente Zufallsprozess der Brownschen Bewegung schnelle Reaktionen fördert. Mit Hilfe der Narrow Escape Theorie kann die mittlere erste Durchgangszeit (mean first passage time) solcher Prozesse auf der Grundlage ihres Reaktionsraums und des Diffusionskoeffizienten bestimmt werden. Die Narrow Escape Theorie von Brownschen Teilchen wird durch einen begrenzten Bereich mit reflektierenden Grenzen und einen kleinen Reaktionsraum gekennzeichnet. In dieser Arbeit wurde die mittlere erste Durchgangszeit in einer Scheibe systematisch als Funktion der Größe der Fluchtöffnung *in vitro* und *in silico* untersucht. Für die *in vitro*-Experimente wurde ein Modellsystem aus strukturierten, Glas gestützten Lipiddoppelschichten (SLB) erstellt. Dieses Modell wurde durch einen kombinierten Kolloid-Metallisierungsansatz hergestellt, bei dem eine strukturierte Goldschicht auf Glas die Bildung von SLB-Scheiben unterschiedlicher Größe durch die Vesikelfusion ermöglicht. Es wurde festgestellt, dass das Modell alle Anforderungen erfüllt, um das Narrow escape problem *in vitro* zu testen. Insbesondere wurde das Reflexionsvermögen der Grenzen, die ungehinderte, freie Diffusion der Lipide und die Präzision der Fläche bewertet. Die beobachteten Ergebnisse der mittleren ersten Durchgangszeit stimmen mit der NEP-Theorie überein. Es besteht eine hervorragende Übereinstimmung sowohl bei den absoluten Werten als auch systematisch über einen Bereich von kleinen Fluchtöffnungsgrößen. Außerdem zeige ich eine einfache Methode, einen Korrekturfaktor, zur Berechnung der mittleren ersten Durchgangszeit aus unvollständigen Lipid Trajektorien des Experimentes. Indem ich die mittlere erste Durchgangszeit auf den Anteil der entkommenen Partikel skalierte, konnte ich die Einschränkungen der Lebensdauer von fluoreszenten Farbstoffen ausgleichen. Mit dieser Technik werden bisher unzugängliche Messungen der mittleren ersten Durchgangszeit auf der Grundlage von fluoreszenten Farbstoffen möglich. In einem umfassenden Ansatz wurden die *in vitro*-Experimente durch verschiedene *in silico*-Experimente ergänzt. Letztere basierten auf Random-Walk-Simulationen in Scheiben, die die *in vitro*-Situation mit ihren Unsicherheiten nachahmten. Die Lebensdauer einzelner Partikel wurde entweder so lang angesetzt, dass alle Partikel entkommen konnten, oder sie wurde so angepasst, dass sie den

in den *in vitro*-Experimenten beobachteten Lebensdauerbeschränkungen entsprach. Ein Vergleich der mittleren ersten Durchgangszeit von unsterblichen Partikeln mit den korrigierten, lebensdauerbegrenzten Partikeln hat die Verwendung des Korrekturfaktors bestätigt. In Übereinstimmung mit der Narrow Escape Theorie wurde experimentell festgestellt, dass die mittlere erste Durchgangszeit unabhängig vom Startpunkt des Teilchens innerhalb der Domäne ist. Dies ist dann der Fall, wenn das Teilchen einen Mindestabstand zur Austrittsstelle einhält. Im Allgemeinen bilden die vorgestellten Random-Walk-Simulationen die in dieser Studie durchgeführten Experimente genau ab. Die erforderliche Hardware für die Einrichtung eines auf Astigmatismus basierenden 3D-Systems wurde in ein vorhandenes Mikroskop eingebaut. Erste Versuche, die gewonnenen 3D-Bilddaten zu analysieren, gaben einen Einblick in das Potenzial der Methode zur Untersuchung der Moleküldynamik im lebenden Trypanosom. Die volle Funktionalität wird mit der laufenden Verbesserung der Bildanalyse außerhalb dieser Arbeit realisiert werden.
Ein Teil der Ergebnisse und Methoden dieser Dissertation wurde zur Veröffentlichung unter dem Titel 'Experiments in micro-patterned model membranes support the narrow escape theory' eingereicht.

# Contents

# 1 Introduction

## 1.1 Brownian motion

Diffusion, the random movement of Brownian particles, is a natural stochastic process for establishing an equilibrium in a fluid or gaseous environment. This movement is driven by thermal energy. In a biological context, a multitude of reactions are based on diffusion. On a small scale, such as in a bacterial cell, diffusion is the most powerful transport mechanism [1]. The motion of a freely diffusing particle is characterized by the diffusion coefficient, $D$. In the case of lateral, one-dimensional diffusion $D$ is defined by Fick´s second law. The following diffusion equation gives the probability of a particle moving in a space with radius, $r$, around an initial point, $r_0$, at time, t,:

$$\rho^{d=1}(r,t) = \frac{1}{\sqrt{4Dt}} \exp\left(-\frac{r^2}{4Dt}\right), \tag{1}$$

where $r^2 = (r - r_0)^2$ [2].

Here, the probability distribution of the individual step lengths, $r$, is Gaussian. A diffusing molecule exhibits periods of free movement interrupted by random directional changes, due to interactions with other particles in the reaction space. Using the model of random motion, we can describe the diffusion process in a simplified way, thereby generating easier access to fundamental questions about diffusion dynamics. In 1905, Albert Einstein showed that the mean squared displacement $MSD(t)$ of a particle moving in an environment with low Reynolds numbers grows proportionally with time [3]. The $MSD(t)$ is typically used to describe displacements with random motion because the $MSD(t)$ exhibits greater robustness in comparison to the investigation of individual displacements. The $MSD(t)$ connects to the diffusion coefficient as follows:

$$MSD(t) = \langle r^2(t) \rangle = \int (\vec{r} - \vec{r_0})^2 p(\vec{r}, t) d\vec{r} = 2dDt \tag{2}$$

In two dimensions we derive:

$$\langle r^2(t) \rangle = 4Dt, \tag{3}$$

resulting in:

$$D = \frac{\langle r^2(t) \rangle}{4t}. \tag{4}$$

The diffusion coefficient can be derived from a fit to the first data points of a $\left\langle r^2(t) \right\rangle$ versus $t$ graph, or a Gaussian fit to the 1D step distribution, as mentioned in Equation 1.

Single molecule trajectories have a limited length due to a multitude of technical causes. Due to the progressive limitation in data availability, the accuracy of individual data points in the $\left\langle r^2(t) \right\rangle$ versus $t$ graph decreases with longer time lags. Accordingly, the use of too many data points in the fit to the $\left\langle r^2(t) \right\rangle$ plot usually negatively impacts the reliability of the result [4]. A rule of thumb to derive a reasonable amount of data points to fit the $\left\langle r^2(t) \right\rangle$ versus $t$ graph is:

$$N_{fit} = \frac{\overline{TL}}{8}, \tag{5}$$

where the mean trace length $\overline{TL}$ determines the number of data points, $N_{fit}$, to include in the fit.

## 1.2 The narrow escape theory and the mean first passage time

A multitude of dynamics in a biological context, as well as in everyday life, can be described by stochastic theory. Temporal properties of the distribution of an infectious disease within a population, the transmission of a neuronal signal [5], and even the progression of the stock market can be addressed using the concept of the first-passage time [6]. The exact first passage time is a random variable and cannot be predicted precisely [6]. The narrow escape theory (NET) gives us the measure to calculate the mean first passage time $\bar{\tau}$ of such processes. In the last two decades, the research conducted on narrow escape processes has experienced considerable progress. As of today, literature on first passage processes has grown to over 7000 hits on the Web of Science [6]. In 2004, the concept of the narrow escape problem was first set in a cellular context by Holcman and Schuss [7]. They developed the first mathematical description of $\bar{\tau}$, which was complemented and extended in the following years for multiple scenarios featuring one or more escape sites, as well as specific geometries of the diffusion domain and escape site [8, 9, 10, 11, 12, 13, 14]. It is safe to say that the NET has been well researched by theoreticians. However, a systematic experimental investigation of the mean first passage time has been missing to date.

### 1.2.1 Calculation of the mean first passage time

The narrow escape theory (NET) describes the passage of a Brownian particle through a small opening in a large enclosure, or an interaction with an equally small target [14]. The rim of the enclosure is reflective everywhere except for the one small escape opening. The narrow escape problem is the mathematical determination of the mean time until escape [14]. This mean first passage time (MFPT or $\bar{\tau}$) is also the inverse of the reaction rate constant [6]. It diverges towards infinity as the escape site size gets closer to zero [14]. Consequently, the experimental exploration of the $\bar{\tau}$ is difficult technically [14]. In a two dimensional system, the mean first passage time depends predominantly on three parameters: (1) the size of the diffusion domain; (2) the diffusion coefficient $D$ of the Brownian particle; (3)

the size of the escape site opening $a$. $\bar{\tau}$ has a strong dependence on the symmetry of the diffusion domain. Experiments from Wei and colleagues indicate that the size of a symmetric diffusion domain, whether round or a square, is the dominating factor contributing to the mean first passage time [15]. This stands in contrast to asymmetric and irregular shapes, which need individual assessment. For the planar environments of a disc, the mean first-passage time is defined as [16]:

$$\bar{\tau} = \frac{r^2}{D}(\ln\frac{1}{\varepsilon} + \ln 2 + \frac{1}{4}), \text{ where } \varepsilon = \frac{a}{C} \ll 1, \tag{6}$$

where the parameter $\varepsilon$ is the relative escape opening defined as the arc length, $a$, of the escape site opening divided by the disc's circumference $C = 2\pi r$. In this study, I will focus on the experimental test of the analytical solution to the NEP for a $2D-$circular domain. Figure 1 illustrates the dependencies of $\bar{\tau}$ under the variation of the three parameters: the logarithmic, proportional and, inverse proportional influence of $\varepsilon$, $r^{-2}$, and $D$ on $\bar{\tau}$, respectively.

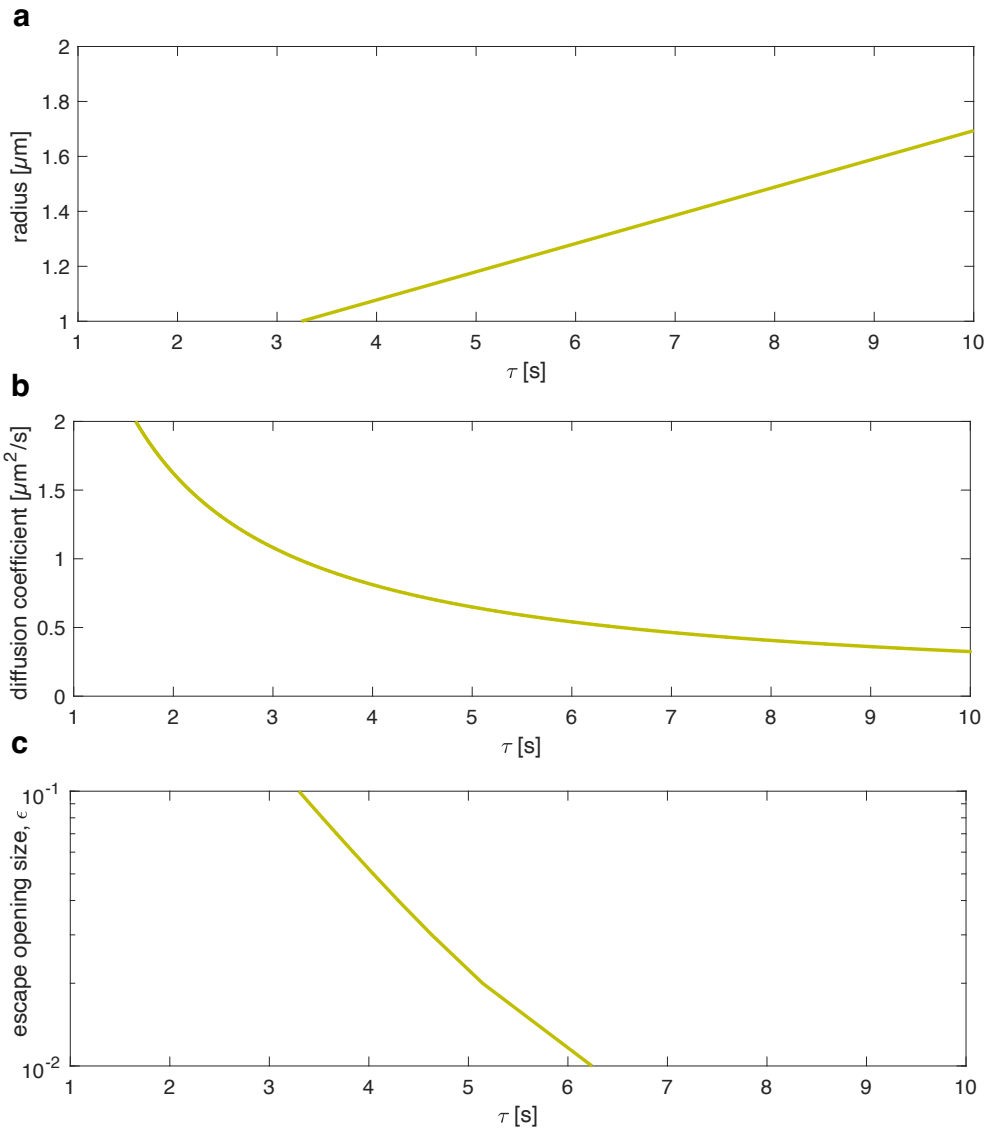


Figure 1: **Overview on the influence of the parameters radius, diffusion coefficient, and the escape opening size, $\varepsilon$ on the mean first passage time according to the theoretical prediction for a disc.** In order of growing influence: **a** The mean first passage time grows proportionally with $r^{-2}$, with constant values of D $= 1\mu m^2/s$ and $\varepsilon = 1\%$. **b** The variation of the diffusion coefficient shows the inverse proportional dependency of $\tau$; $\varepsilon$ and $r$ are constant at $1\%$ and $1\mu m$. **c** The escape opening size has a logarithmic influence on $\bar{\tau}$, where $D$ and $r$ are constant at $1\mu m^2/s$ and $1\mu m$.

From the scientific literature we know that the escape times are exponentially distributed [16]. Experimentally, the mean first passage time is derived from an ex-

ponential fit of individual escape times of Brownian particles in a disc. Figure 2 illustrates an exemplary trace of a Brownian particle diffusing in a circular domain and escaping through a small opening at the top the confinement.

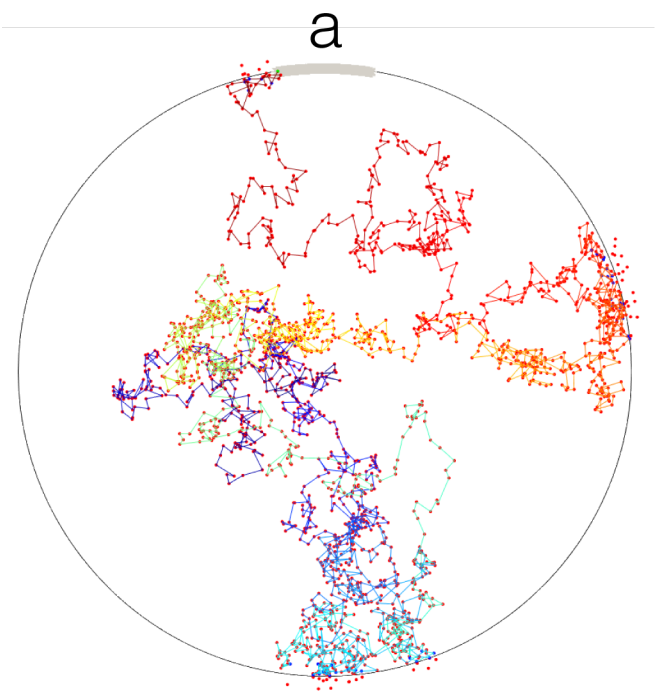


Figure 2: **Narrow escape from a disc.** Depiction of a simulated single particle trace in a confining disc. The single particle was performing Brownian motion and was reflected at the interaction with the disc's boundary. The movement was terminated upon hitting the escape site $a$ marked in gray. The time is color-coded ascending from blue to red, with red dots marking individual time points. Red dots outside the diffusion disc mark hypothetical particle positions without the application of the reflection. The point of escape is marked with a green dot on the gray escape site.

## 1.3 Membranes as models

Model membranes can mimic the plasma membrane of the cell. In such a model, the complexity of the original system is simplified and the model provides a defined environment where all parameters are known and can be manipulated. Model membranes can be built using various techniques, including several different lipids and the optional integration of proteins and other substitution molecules [17, 18, 19]. The amphiphilic nature of lipids due to their hydrophilic head-group and hydrophobic tails mediate the characteristic organization of a group of lipids in an aqueous medium into micelles and vesicles. A vesicle is probably the simplest version of a model membrane system. With vesicle rupture, planar models such as the supported lipid bilayer (SLB) can be formed on a support. An option that allows tighter control of the SLB formation is the use of the Langmuir-Blodgett [20] or the Langmuir-Schaefer methods [21], where a planar layer of lipids is transferred to a glass support. These planar systems have great advantages in imaging. Due to the small height and the reduced fluctuation in the membrane, observations can usually be made in one imaging plane. The membrane can be described as a two-dimensional liquid [22] with free lateral movement [23]. Plasma membrane compositions can be immensely diverse, consisting of up to 500 different lipids [24]. The lateral self-organization can lead to phase separation in lipid bilayers [25]. Phase separation can modulate diffusion coefficients and compartmentalize the plasma membrane [26, 27, 28]. The most common groups of lipids in cellular membranes are phospholipids, sphingolipids, and sterols, with cholesterol being especially known for increasing rigidity [29]. The abundance of the different groups is function-dependent and differs between cellular organelles and the plasma membrane [30]. The limitation to one or a small number of lipid types supports a consistent diffusion coefficient. This is especially beneficial in model membranes. In this study, a planar SLB was used to test the narrow escape theory for a 2D scenario. The model was chosen due to its accessibility, low cost, as well as advantages in imaging. The model membrane consisted of two phospholipids, predominately SOPC (1-stearoyl-2-oleoyl-sn-glycero-3-phosphocholine) lipids with a trace amount of DOPE-Atto647N (1,2-dioleoyl-sn-glycero- 3- phosphoethanolamine with Atto647N label) lipids carrying the fluorescent label on their head groups.

## 1.4 Micro-structuring in model membranes

The task of generating model membranes with distinct geometries can be approached from multiple angles. As mentioned above, lipid mixtures undergo self organization. This self organization can then be used to generate patches in a solid supported lipid bilayer. According to the lipid mix used, the diffusion properties could be modulated and differ from the surrounding bilayer. Vesicle rupture of giant unilamellar vesicles on a planar glass substrate yields the potential to create irregularly-shaped patches. Giant unilamellar vesicle (GUV) rupture on a porous structure was reported to be a simple tool to create free-standing bilayers in the micrometer range [31]. Interestingly, Groves described a method of membrane printing as early as 1997 [32]. Here, gold, aluminium oxide, and a photo-resist were tested as substances to generate micro-patterned membranes. The photo-resist was found to be the most suitable material, due to its non-conductive properties and the advantages in preparation. Selective development of the resist through a photo-mask allowed the creation of corralled arrays from 5 to 200 $\mu m^2$. In this case, the membrane was introduced to the resist scaffolds by vesicle fusion. Though the separation of the individual membrane patches was demonstrated, single-molecule dynamics and the reflective properties of the resist barriers were not investigated. In fact, the reflectivity of the boundaries is crucial to unhindered diffusion and therefore must be ensured for testing the NEP. Boundary-free approaches are a way to circumvent hindered reflection due to rough or sticky interfaces entirely. Isolated lipid bilayer patches can be created by short-wavelength ultraviolet radiation, which are able to etch a desired pattern into a lipid bilayer [33]. To circumvent the void introduced by the etching, UV cross-linkable lipids can be used to build a rigid lipid boundary around an intact membrane patch [34]. The etching of distinct shapes requires a chromium photo-mask, similar to the above techniques using photo-resist. When a photomask is used to generate a structured scaffold or a structured bilayer directly, the resolution is affected by the quality of the illumination through the mask. Close contact with a minimum distance of the substrate to the photomask is required. In the case of structuring after the formation of the lipid bilayer, this can temper the quality of the membrane. This project focuses on a method where the lipid bilayer is introduced onto a gold-structured substrate. From a technical point of

view, the substrate can be any metal that can be evaporated. To create distinct shapes, such as the circular wells in the substrate, the metal is evaporated onto polystyrene colloids randomly distributed on glass. Upon removal of the beads, the metal coat forms a high-resolution boundary layer around empty wells. Gold is relatively bio-compatible and chemically inert [35]. The adhesive properties are not optimal, but can be sufficiently enhanced by an adhesion promoter in the form of a thin layer of titanium [36]. Gold can then be functionalized with 1-dodecanethiol to introduce hydrophobic properties. The functionalized gold forms a barrier for membrane formation due to its hydrophobicity and shows minimal adhesion forces to the lipid bilayer [37]. These properties make this approach an ideal model system to test diffusion in membrane patches.

## 1.5 Single-molecule fluorescence microscopy

The resolution of light microscopy is limited by the diffraction limit of light. It is influenced by the numerical aperture of the objective in the microscope and by the wavelength of light which forms the image. Building on the observations of George Airy in 1835, Ernst Abbe formalized the diffraction limit mathematically in 1873 [38]. The Abbe limit describes the minimal distance, $d$, in which two lines need to be apart in order to be resolved by a light microscope [38]:

$$d = \frac{\lambda}{2nsin\theta} = \frac{\lambda}{2NA}, \tag{7}$$

in terms of the wavelength of light, $\lambda$, and the numerical aperture of the objective, NA. The latter of these is defined as 2 times the reflective index of the optical medium, $n$, multiplied by the sine of the half aperture angle, $\theta$, from the objective. In the example of a far-red emitter and the microscope used in this study, the diffraction limit is calculated as: $d = \frac{647nm}{2.8} = 230\,nm$.

In the case of a single fluorescence emitter, the Rayleigh criterion can be applied to determine the diffraction limit [39] from the central spot of the point spread function (PSF), which contains more than 80 % of the information [40]. The center of this so-called Airy disc can be localized with a higher precision than the whole emitter profile. Individual emission profiles can be distinguished if the distance of the centers of both intensity maxima is greater than the radius of the maximum. The required distance can be obtained from [39]:

$$d = \frac{0.61\lambda}{NA}. \tag{8}$$

A great number of biological structures on the single molecule level range below the size of 200 $nm$. Therefore they are, by the Abbe limit or the Rayleigh criterion, out of reach for light microscopes. One way to go beyond this limit is to employ short wavelength electrons instead of visible light [42]. Despite its immense advantages (resolution down to 1 Å), electron microscopy is still not able to image living cells or dynamics. The high energy of the electron beam, the vacuum, and the often

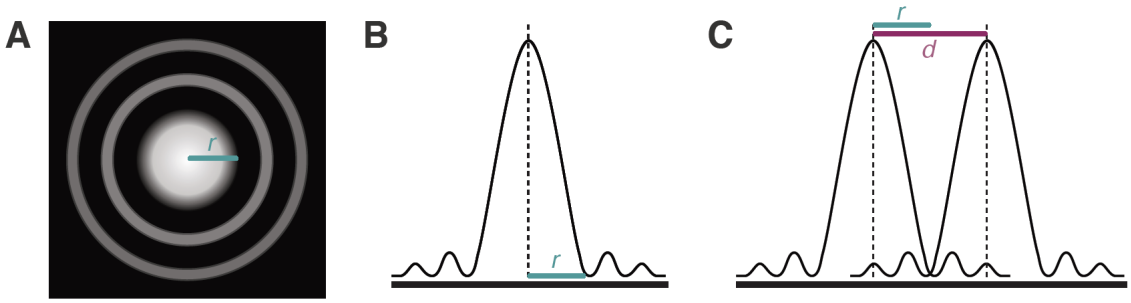


Figure 3: **The Rayleigh criterion**. **a** Idealized diffraction pattern (PSF) of a single emitter through a circular aperture, top view. **b** Schematic side view of the PSF with the characteristic side maxima. **c** Two diffraction patterns can be localized if the distance $d$ of the centers of the Airy discs is greater than the distance of $r$, with $r$ marking the radius of the Airy disc. This figure is adapted from [41].

obligatory contrasting methods using heavy metals are harmful to live biological specimens [42, 43].

There are different approaches to bypass the Abbe limit in light microscopy. One method, used since the early 1990s, is based on the dilution of the label. The resulting low concentration of the fluorophore allows the precise detection of single, distinguishable emission profiles. The Airy disc is a 2D representation of the maximum of the characteristic emission profile of a single emitter. By determining the center of the Airy disc, localization precision beyond the diffraction limit can be achieved [44, 45]. The dilution of the signal can be realized by either limiting the number of fluorophores in the sample, by spatiotemporal separation caused by using fluorescent proteins with stochastically switching on- and off-states [46], or by a mix of distinguishable colors. In this study, the sufficient separation of the fluorescent label was ensured by simple dilution.

### 1.5.1 Detection of super-resolved single particle dynamics

A method to investigate single-particle dynamics is single-molecule tracking. To achieve efficient single-molecule tracking, a high temporal and spatial resolution is key. To resolve dynamics, a single emitter must be localized in consecutive images of a movie. Reliable localization algorithms have been developed and optimized over

the last decades. The most common approach is to fit a Gaussian profile to the PSF to determine the center of the emitter [40]. The achievable imaging speed and localization precision depend on the number of photons available. Another prerequisite for successful localization is a sufficient signal-to-noise ratio [47]. The signal-to-noise ratio (SNR) is usually found to be sufficient if the ratio between the detected signal and the variation in the background is $> 8$ [48]. For the data obtained in this study a mean SNR of 18 was calculated accordingly to Ober [49]. Several values contribute to the background detector noise in electron-multiplying charge-coupled device (EMCCD) technology, with the most common being dark current noise, shot noise, multiplicative noise, and spurious noise. A high background noise is not necessarily crucial to the analysis, but high fluctuations are. Dark current noise can result in detector-specific patterns and originate from currents within the detector, not from entering radiation [50]. This can be reduced by cooling the camera. Shot noise is caused by natural fluctuations in the number of photons emitted by the light source. As with shot noise, multiplying noise results in a variation in the amount of detected photons. Here, the noise is caused by uncertainties in the signal multiplying process. When imaging biological samples, the autofluorescence of the cell, which is expected at an emission of $\lambda_{max} = 520\ nm$, needs to additionally be considered [51]. To separate the background noise from the actual signal, several steps are performed in image processing [2]. Noise which is constant during the acquisition, for example dark current noise, can be imaged prior to the actual measurement. The averaged pixel intensities can then subsequently be removed during the acquisition. During image analysis, all remaining signal is cross-correlated with the pattern of the diffraction-limited single emitter profiles [2]. The approximation of the PSF by a Gaussian fit allows the deduction of its intensity and signal width [23]. Known properties of the used label allow a threshold to be set in order to identify single-molecules, in contrast to other detected signals and noise. Subsequently, the remaining peaks are fit to deduce the coordinates on the camera chip. Tracking algorithms allow the connection of single-molecule localizations over time. Efficient tracking of single molecules is limited by the localization precision, $\sigma$, which is predominately set by the number of photons, $N_\gamma$, detected from a fluorophore. Thompson calculated an expression of $\sigma$ which additionally regards pixel size, $a$, background noise, $b$, and the width, $\omega$, of the fit PSF [52]:

$$\sigma = \sqrt{\frac{\omega^2}{N_\gamma} + \frac{a^2/12}{N_\gamma} + \frac{8\pi\omega^4 b^2}{a^2 N_\gamma^2}}. \tag{9}$$

To acquire a sufficient amount of photons for a satisfactory spacial resolution, it can be necessary to extend the illumination time and therefore limit temporal resolution. To improve $\sigma$, dyes that exhibit a high fluorescence quantum yield are an advantage. The fluorescence quantum yield, $\Phi_f$, defines how many photons a fluorophore emits per photon absorbed,

$$\Phi_f = \frac{\gamma_{emitted}}{\gamma_{absorbed}}. \tag{10}$$

Aside from the photon count, $\sigma$ can also be determined using the standard deviation of a Gaussian fit to the PSF or from an immobile single emitter.

### 1.5.2 3D single-molecule fluorescence microscopy

As described above, using wide-field fluorescence imaging one can study single-molecule dynamics in a plane. The use of this technique is widespread and well-established. It is especially powerful in experiments at the plasma membrane or in planar model systems such as the SLB [2]. In the three-dimensional context of the cell, an additional important clue to investigating molecule dynamics is the axial information. Currently, there are many ways to achieve 3D information at the single molecule level. The simplest but probably least efficient method is homogeneous off-focus imaging [53]. Engineered point-spread functions (PSF) lower the negative effects of the off-focus blur by introducing directionality. Multi-plane imaging is another method worth noting. Several detectors or parts of a camera chip are used to distinguish light emission from different focal planes [54]. This technique can be combined with super-resolution microscopy methods [55]. Due to the spread of the photons to the different planes, the localization precision will be lowered in comparison to a single plane, and therefore solutions to ensure sufficient photon emission must be considered. A third method to increase the axial information is the generation of a so-called double-helix PSF. This type of engineered PSF exhibits two lobes, twisted around an optical axis, with the direction of the movement indicating

the position above or below the focal plane [56, 57]. Unlike the off-focus imaging or the astigmatism based single-molecule fluorescence microscopy (3D SMFM) method, the PSF does not expand along the optical axis, but the axial information is stored in the angle that the lobes are positioned towards each other. Therefore, it lowers the loss of precision due to the limitation of photon numbers. However, the introduction of a double-helix PSF requires a phase mask in the Fourier plane. An approach dating back to Kao and Verkman in 1994 [58] which was further improved and tested with tracking of quantum dots [59], uses the astigmatic deformation of the PSF to obtain axial information on the emitter position. Here, the shape of the deformation encodes the axial position of the single particles. One big advantage of this method is that 3D information can be gained without moving the specimen or the microscope, which also increases temporal resolution. A prominent example of another application of this method is found in the work of Huang and colleagues from 2008. They combined stochastic optical reconstruction microscopy (STORM) with a weak cylindrical lens, introducing an astigmatic deformation to the PSF. They thereby obtained structural information in 3D on the single molecule level [60]. From test data, we know that average spatial resolutions of 26 to 28 $nm$ (planar) and up to 29 to 66 $nm$ (axial) [61] and a temporal resolution with an imaging speed of up to 200 Hz (0.005 s) are to be expected in an optimal case. The focal length of $f = 1\ m$ is proposed to provide an imaging depth of up to 1 $\mu m$. The imaging depth is tied to the distance of the two foci caused by the cylindrical lens. A calibration curve can be used to determine the axial position from the astigmatic deformation. This curve or look-up-table is usually generated by imaging fluorescent emitters at a gradient of positions, which is precisely set by a Piezo-positioning device.

In a side project, I set out to implement an extension to the existing custom microscopy setup that would allow axial information to be obtained for single molecules. In theory, the most cost-efficient and easy-to-install method is PSF engineering via the introduction of a weak cylindrical lens into the emission beam path right before the camera. This approach is inspired by the work of Kao and Verkman [58], Holzer [59], and Huang [60].

### 1.5.3 Fluorescent labels in single-molecule fluorescence microscopy and live-cell imaging.

Labels used in single-molecule fluorescence microscopy (SMFM) need to meet specific requirements which are determined by the technique itself and the research question at hand. Extreme photo-stability, as suggested for the analysis of the mean first passage time, $\tau$, is found in gold beads [62] and nanodiamonds [63, 64]. There is also the advantage that neither produces any toxic effects and can be used with a wide range of surface modifications [64]. Common disadvantages include: i) their large sizes, as these particles can interfere with the dynamics under investigation, especially in crowded biological environments; ii) gold particles may heat during observation, introducing perturbations [65]; iii) unspecific interactions and cross-linking of proteins [66], which can modify the system. Techniques that do not require labels can alleviate some of these restrictions. The method of interferometric scattering microscopy (iSCAT) offers an excellent example of what can be done. Label-free iSCAT is however restricted to *in vitro* experiments [67]. In live-cell imaging, fluorescent proteins are frequently the first choice [34, 68]. Fluorescent proteins are available in a great variety of emission spectra [69]. They can be introduced into the organism at the genome level, where a direct fusion to the gene of interest promotes the specificity of the labeling technique. Further, the possibility to induce the labels' expression, photo-activation, and photo-conversion are all valuable tools [70, 71]. Blinking or bleaching, as found with some fluorescent proteins, can, however, impede fluorescent label traceability [65]. Fluorescent protein labels can interfere with folding, localization, and protein dynamics due to their large size [72]. There are several advantages to using organic dyes over fluorescent proteins, including their smaller size, minimal interference with experiments, and greater photostability. In this study, single-molecule fluorescence microscopy was employed to analyze single-particle dynamics in model membranes. The aspect of reliable localization and traceability as well as sufficiently long observation times of single traces is essential to test the narrow escape theory. In narrow escape scenarios, most dyes (even those with emission spectra far from the autofluorescence of biological samples [73] and immense photo-stability [74]) miss escape events. Nevertheless, we chose the commonly-used label ATTO647N as a tracer to test the narrow escape problem.

How the mean first passage time was determined despite the missing long escape times will be described later.

## 1.6 Aim

This thesis aims to take a holistic approach to systematic testing of the narrow escape problem in a disc, both experimentally and using random walk simulations. The experiments were conducted in a model system established for this purpose. It consisted of micrometer-sized membrane patches with defined radius and reflective boundaries. Single fluorescent lipids were tracked at high spatial and temporal resolution to determine their mean first passage time, $\tau$, as a function of the escape opening. In this thesis I propose a solution to the well known problem of fluorescence lifetime limitation in single-particle tracking in the context of the determination of $\tau$. The limitation was overcome by re-scaling the measured mean first passage time with the fraction of escaped particles. By comparison of random walk simulations featuring lifetime limited and immortal particles, the theoretically-predicted solution was proven successfully. This solution provides the opportunity to investigate single-molecule dynamics and examples of the narrow escape problem also in living cells, such as *Trypanosoma brucei*, where short traces are unavoidable due to the small size and high curvature of the cells. Additionally, it is necessary to track the particles in 3D. Thus, an astigmatism based 3D single-molecule tracking setup was implemented and characterized.

# 2 Materials and Methods

## 2.1 Materials

### 2.1.1 Chemicals and solutions

Table 1: **Chemicals and solutions.**

| Item | Supplier |
|---|---|
| Trichlormethane (chloroform) | Sigma-Aldrich, St. Lewis, (MO) |
| Acetone (99,5%) | Sigma-Aldrich, St. Lewis, (MO) |
| Ammonia Solution (32%) | AppliChem, Darmstadt (GER) |
| Ethanol | Carl Roth, Karlsruhe (GER) |
| Hellmanex 3 | Hellma Analytics, Müllheim (GER) |
| Hydrogen Peroxide (30%) | AppliChem, Darmstadt (GER) |
| Methanol | Carl Roth, Karlsruhe (GER) |
| Sulphuric acid (96%) | Carl Roth, Karlsruhe (GER) |

Table 2: **Buffer.**

| Item | Composition |
|---|---|
| Hellmanex cleaning solution | 2% Hellmanex 3 |
| | ddH2O |
| Vesicle buffer, NTC | 20 mM Tris-HCl pH 7.6 |
| | 50 mM NaCl |
| | 0.5 mM CaCl2 |

### 2.1.2 Lipids

Table 3: **Lipids.**

| Lipid Name | Label | Manufacturer |
|---|---|---|
| SOPC | - | Avanti Polar Lipids, Alabaster (AL) |
| DOPE | ATTO 647 N | Avanti Polar Lipids, Alabaster (AL) |

### 2.1.3 Equipment, instruments and materials

Table 4: **Equipment.**

| Item | Supplier |
|---|---|
| Aluminum foil | Carl Roth GmBH, Karlsruhe (GER) |
| Cover glasses, | Karl Hecht GmbH &Co KG, |
| 22x22 mm 0.17 ± 0.01 mm | Sondheim (GER) |
| PTFE Syringe Filters 0.22 $\mu$m | Hartenstein Laborversand, Würzburg (GER) |
| Syringes | Hartenstein Laborversand, Würzburg (GER) |
| Syringe needles | Hartenstein Laborversand, Würzburg (GER) |
| Expanded Plasma Cleaner 230 V | Harrick Plasma (NY) |
| Sonicator Elmasonic P30H, 320 W | Elma Electronic Inc. (CA) |
| Hamilton Syringe | Sigma-Aldrich, St. Lewis, (MO) |

Table 5: **Hydrogel.**

| Item | Manufacturer |
|---|---|
| 8-arm PEG-Vinylsulfone | Sigma-Aldrich |
| (10 kDa, tripentaerythritol core) | (St. Louis, USA) |
| Thiol-functionalised hyaluronic acid | Leonard Forster |
| (HA-SH), 40% substituted, 10 kDa | (AG Groll, University of Würzburg) |

### 2.1.4 Optics and Microscope-related devices

Table 6: **Optics and Microscope-related devices.**

| Item | Supplier |
|---|---|
| Leica DMI6000B | Leica, Wetzlar (GER) |
| Cobolt Fandango 515 $nm$, 50 $mW$ | Hübner photonics, Kassel (GER) |
| Cobolt MLD 640 $nm$, 100 $mW$ | Hübner photonics, Kassel (GER) |
| AOTF nc-400.650-TN | AA opto-electronic, Orsay (FRA) |
| HCX PL APO 100x/ 1.47 OIL CORR TIRF | Carl Zeiss, Oberkochen (GER) |
| iXon3 DU-897 | Andor Technology, Belfast (NIR) |
| dichroic filter, zt405/ 514/ 633rpc | Chroma, Rockingham (AU) |
| emission filter, 550/49 BrightLine HC | Semrock, IDEX, Rochester (NY,USA) |
| Shutter,VCM-D1 | UniBiltz, Rochester (NY,USA) |
| P-721.SL2 PIFOC Piezo z-stage | Physik Instrumente, Karlsruhe (GER) |
| E-709 Digital Piezo Controller | Physik Instrumente, Karlsruhe (GER) |
| N-BK7 Plano-Convex Lenses | Thorlabs, |
| (AR Coating: 400 - 1100 $nm$) | Newton (NJ,USA) |

### 2.1.5 Software

Table 7: **Software.**

| Software Name | Provider |
|---|---|
| MATLAB R2014a, R2017a | The Math Works Inc., Natick, (USA) |
| TeXShop | University of Oregon, Eugene (USA) |
| MicroManager 1.4/2.0 | Vale lab, US National Institutes of Health (USA) [75] |
| GitHub | GitHub, Inc., San Francisco, (USA) |
| Cobolt Monitor | Cobolt, Solna, (SWE) |
| Microsoft Office | Microsoft, Redmond, (USA) |
| BLAST | National Center for Biotechnology Information |
| ApE | M. Wayne Davis [76] |

## 2.2 Methods

A part of the listed methods was already used and described in [77], Sections marked with an asterisk are direct citations.

### 2.2.1 Preparation of glass coverslips

The following protocol was used to ensure the hydrophilic properties of the microscopy coverslips. Glass coverslips 22x22 of a controlled thickness of $0.17 \pm 0.01mm$ (Karl Hecht, Sondheim (GER)) were plasma cleaned with ambient air (Expanded Plasma Cleaner 230 V, Harrick Plasma (NY)) at a high power setting (30 W) for 20 minutes. The glass was cleaned thoroughly with dd$H_2O$, followed by acetone, ethanol, and methanol sonication (10 min at 37 kHz) for 10 minutes each. The glass coverslips were thoroughly washed with dd$H_2O$ whenever the solvent for the sonication was changed. After 45 minutes of immersion in RCA solution (1:1:5, ammonia: hydrogen peroxide: ddH2O) at 80°C, the coverslips were washed with at least 1 L dd$H_2O$ as the final step of the cleaning protocol. It is recommended not to use clean and hydrophilic glasses after three days of storage [77].

### 2.2.2 Micro-structuring of glass coverslips

In order to structure glass coverslips on a microscopic scale, colloidal lithography was employed. Polystyrene beads ($r_{bead}$=2.5 $\mu m$) were placed on hydrophilic glass coverslips. The specimen was coated with titanium as an adhesion promoter. In the following step, a gold layer of 100 $nm$ was applied by metal evaporation. The polystyrene beads were subsequently washed off with dd$H_2O$ from a syringe. After the removal, the substrates exhibited a gold layer with irregularly distributed glass-bottomed wells of the precise shape of the beads. Figure 4 illustrates the protocol for micro-structuring of glass.

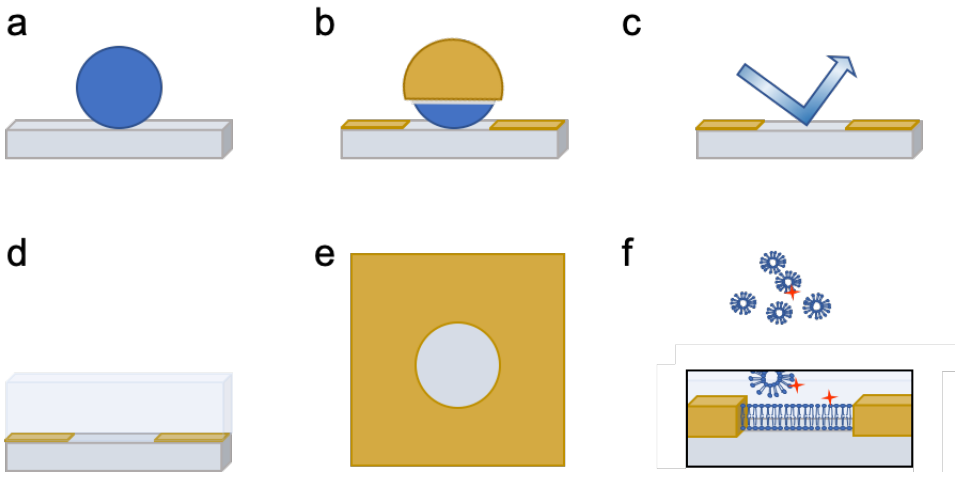


Figure 4: **Mixed colloid-metallization technique for preparation of micro-structured surfaces. a** Deposition of the colloids. **b** Metal evaporation of titanium and gold followed by **c** removal of the colloids by rigid washing. **d** Scaffolds were cleaned and stored in NTC buffer. **e** Top view and **f** side view of a scaffold/ membrane patch after introduction of a SLB from vesicle fusion.

### 2.2.3 Preparation of micro-structured membranes

Vesicle fusion was used to prepare micrometer-sized SLBs of a defined radius in the wells of the gold scaffold described above. A custom observation chamber was built with the scaffold as the glass bottom and a Teflon washer forming a cavity on top. This setup allowed the preparation of the SLB in an aqueous solution, and imaging through the glass bottom of the scaffold with an inverted microscope. Small unilamellar vesicles (SUVs) were prepared from SOPC (1-stearoyl-2-oleoyl-sn-glycero-3-phosphocholine) or a mixture of SOPC and DOPE ATTO 647N (1,2-dioleoyl-sn-glycero-3-phosphoethanolamine), Avanti Polar Lipids, Alabaster (AL). The chloroform-dissolved lipids were dried under a nitrogen stream and subsequently rehydrated in NTC buffer by briefly vortexing them. The NTC-lipid-mix was then sonicated (37 kHz) for 10 minutes in pulsed mode, and then for 10-30 minutes in sweep mode. During sonication, ice was used to maintain temperatures below 20 °C. Membrane patches were formed by incubating SOPC SUVs on micro-structured glass for a minimum of 1 hour at 37 °C. Excess vesicles were removed by washing with 20

ml NTC buffer, ensuring that the membranes did not become dry. SUVs prepared from SOPC (0.005 mol % DOPE ATTO 647N labeled lipids) were incubated with pre-formed SLBs to introduce trace amounts of fluorescently-labeled lipids. It was usually not necessary to use more than a 1-5 $\mu$l of a 1 mg/ml SUV solution. Washing with 20 ml of NTC removed excess vesicles. The exact number of lipids in a disc can only be estimated. With a mean size usage of a lipid headgroup of 0.7 $nm^2$ and the mean area of the membrane discs of 18.7 $\mu m^2$ [78], a total of 27x$10^6$ SOPC molecules per disc including around 10 labeled DOPE molecules can be expected. The labeling of lipids amounts to approximately 0.3 parts per million. The micro-structured membrane on glass was imaged at 25 °C on the same day. For long-term storage, lipid stocks were stored dry at -80°C. For short-term storage, lipids were kept in chloroform (HPLC grade, Carl Roth, Karlsruhe (GER)) and stored at -20 °C, previously described in [77].

### 2.2.4 Functionalization of micro-structured gold

Functionalization of the gold substrates was done overnight by incubation in 0.1 mM 1-dodecanethiol in ethanol. Prior to use, the substrates were immersed 3 times in 70 % ethanol followed by one wash in dd$H_2O$. After functionalization, the substrates were never allowed to become dry during experiments.

### 2.2.5 Immobilization and sample embedding in hydrogel

To investigate single-molecule dynamics in living cells it is imperative to immobilize the specimen while still ensuring cell viability. A tool which was found to be suited for *T.brucei* is a hydrogel based on 8-arm poly(ethylen glycol)-vinyl sulfone (PEG-VS) and thiol-functionalised hyaluronic acid (HA-SH). It was first evaluated by M. Glogger [79] and further refined by M. Schwebs [41]. When used in this study, the protocol followed the protocol developed by Schwebs.

### 2.2.6 Single-molecule imaging

Single-molecule imaging data was obtained with an in-house custom microscopy setup as described in [77]. The Leica DMI6000B inverted wide-field microscope was equipped with laser lines of 515 $nm$ (Cobolt, Fandango, 50 mW), 640 $nm$ (Cobolt, MLD, 100 mW), an acousto-optical tuneable filter AOTFnc-400.650-TN (AA opto-electronic, Orsay), and a high numerical aperture objective (HCX PL APO 100x/ 1.47 OIL CORR TIRF, Zeiss). The emission light was separated by a dichroic mirror (F48-635, Chroma) in the OptoSplit (CAIRN), enabling sequential imaging. A back-illuminated EMCCD camera, (iXon3 DU-897, Andor Technology, Belfast) was used for signal detection with appropriate filters (zt405, 514, 633rpc (dichroic, Chroma, Rockingham), 550/49 BrightLine HC (emission filter, Semrock, Rochester) and 698/70 BrightLine HC (emission filter, Semrock, Rochester). Movies of up to 10,000 frames were taken in crop mode at 100 Hz with a frame size of 95 x 95 px. (image pixel size was 160 $nm$ and a laser intensity of 1 kW/cm$^2$) with pulsed illumination. Here, an illumination time of 9 $ms$ and a time lag of 10 $ms$ were applied. The AOTF opening was triggered by the camera-ready signal to ensure synchronized sample illumination and camera readout. The open-source software $\mu$Manager 1.4 [75] was used to control the image acquisition process. Background subtraction was performed by using the flat field correction tool integrated into the $\mu$Manager software. To this end, 100 consecutive images were captured by the camera chip without illumination. The average of all frames was calculated using FIJI and subsequently used for background subtraction.

### 2.2.7 Analysis of single-molecule localizations

All analysis of single-molecule imaging data was done using custom MATLAB (The MathWorks Inc., Versions: R2013a-R2019a) routines. The first steps in the analysis: localization and particle tracing have been described previously [2, 23].

#### 2.2.7.1 Localization of single emitters

In order to determine the localization of single emitters in the microscopy data with high spatial accuracy, their intensity distributions were fit with a 2D Gaussian function. The fit yielded the width and integrated intensity of the single emitters as well as the errors of all parameters. The found positions were filtered with respect to the likelihood to fit to the known characteristics of the used dye, ATTO647N, under the same illumination conditions. The list of positions cleared to this extent served as the input for the tracking algorithm.

#### 2.2.7.2 Tracking of single emitters

The single-molecule positions in adjacent frames of a movie were connected using a probabilistic algorithm. Based on the assumption of free diffusion, a translation matrix was constructed to analyze potential connections. By maximizing the probability of all connections, the trajectories were connected. ATTO647N-labeled lipids were localized with an accuracy of $\sim 20\ nm$ on solid-supported lipid bilayers on micro-patterned glass. Refer to [2] for details.

### 2.2.8 Analysis of single-molecule traces

Image data from preparations that did not yield fluent membranes were excluded from the analysis. Data exclusion was determined based on the occurrence of immobility, indicating defects in the membrane. Additionally, a clearly distinct fraction of extraordinarily slow traces that could not reach the escape site within the observation window were excluded in order to prevent bias in the mean first passage time analysis.

#### 2.2.8.1 Separation of mobile and immobile traces

Immobility of lipids in a solid-supported lipid bilayer is recognized as a preparation artifact. To remove immobile particle traces from the diffusion analysis, the enclosing squared displacement (SD) was used as a measure. The threshold of SD

to distinguish immobility was found in two complementary steps. First, all SD, in units $4 * \sigma^2$, were sorted in an ascending list and plotted on a line plot. Characteristic changes were annotated manually. In this way, a preliminary threshold was defined. In the second step, all traces were plotted in an array with respect to their enclosing SD. Usually, the transition of immobile traces to mobile traces was easy to distinguish and matched the preliminary threshold. The SD of the first 5 immobile traces was determined and the mean was used as a threshold. This mean value was considered a reasonable threshold to separate traces.

#### 2.2.8.2 Determination of immobile-area fraction

To judge the membrane quality, the proportion of defects was examined. The trajectories were sorted in immobile and mobile trace parts. The fraction of the area covered by immobile traces with respect to the total area of the membrane patch was determined with a custom Matlab function. The resolution limit was the pixel size of the recording.

### 2.2.9 Experimental determination of the mean first passage time

#### 2.2.9.1 Collection of escape times from single particles

The micro-patterned SLB exhibited no physical escape site for single particles. In order to gradually and precisely vary the escape site opening size, the escape sites were set virtually in the analysis as follows. The circumference of each membrane patch was divided into escape openings of various sizes, always covering the entire boundary. To collect the escaped particles, one opening after the other was used, with only one escape opening being open at a time. Thus, bias in choosing a single site was excluded while the microscopy data was exploited to a maximum. If a particle trace co-localized with the escape opening, it was counted as escaped. Traces leading both to and from the escape site were analyzed since the Brownian particle has no memory. The escape time was calculated using the number of steps and the time lag of the acquisition.

#### 2.2.9.2 Extraction of the mean first passage time from exponential fit to ET distribution

The mean first passage time was extracted from the fit to the exponential tail of the probability density histogram of the escape time distribution. The exponential tail was found automatically by minimizing the value for $R^2$ in the fit, as described in [77]. Figure 5 shows a representative example.

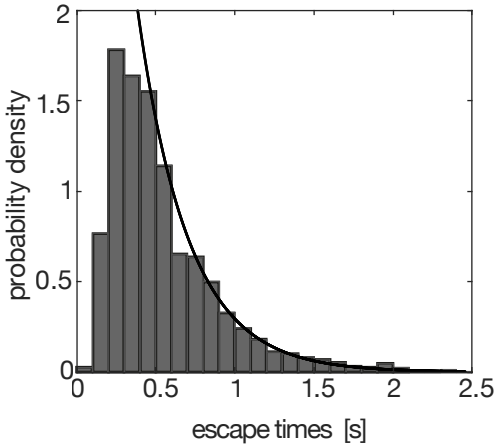


Figure 5: **A fit on the exponential tail determines the MFPT.** The mean-first passage time was experimentally determined from a fit (black line) to the exponential escape time distribution (gray bars). This example shows the escape time distribution of particles defined to a domain with radius 2.44 $\mu m$, a diffusion coefficient of $2.29 \mu m^2/s$, and a escape site size of 1 %. The fit resulted in an escape time of 0.4 s.

### 2.2.10 Estimating the escape time from incomplete trajectories *

The experimental approach to measure the mean first passage time $\tau$ was limited by the lifetime and traceability of the used fluorescent emitter, here ATTO 647N. During the time of observation $T$, the trajectories disappeared at random. Consequently, the total number of trajectories $n_T$ recorded per domain was much larger than the number of absorbed trajectories $n_a$. The absorbing probability $p$, which represents the probability that a trajectory is absorbed before it disappears, can be computed from the fraction of absorbed trajectories. The absorbing probability is

defined and approximated by the formula:

$$p = P\{\tau_a < \tau_k, \tau_a < T\} \approx \frac{n_a}{n_T}. \tag{11}$$

We used this absorbing probability to derive the relation between the theoretical narrow escape time $\bar{\tau}_{th}$ and the $\bar{\tau}_{exp}$ estimated from experimental trajectories. The absorbing probability $p$ provided a correction factor for the time $\bar{\tau}_{exp}$, which is relevant especially if the mean duration of the trajectories is much shorter than the absorbing time $\bar{\tau}_{th}$, as observed here.

To derive the relations between these parameters, we recall that the mean first passage time $\langle\tau_d\rangle$ for a particle that disappears has two components: one due to absorption at the narrow window, and the second due to fluorophore killing or bleaching. Thus, since the two events are independent, using Bayes'law, we obtain:

$$\langle\tau_d\rangle = (\tau_a|\tau_a < \tau_k)p + (\tau_k|\tau_k < \tau_a)(1-p), \tag{12}$$

where $\tau_a$ and $\tau_k$ is the first absorbing and killing time, respectively. We assumed that the end time $T$ is sufficiently long and ignored the remaining particles that could not be absorbed or killed after time $T$. This result was independent of the killing law for trajectories [14].

When the killing time was much smaller than the absorbing time, $\langle\tau_k|\tau_k < \tau_a)\rangle \ll \langle\tau_a|\tau_a < \tau_k\rangle$, we ignored the second term, in Equation 12 and thus were left with the relation $\langle\tau_{th}\rangle = \langle\tau_a|\tau_a < \tau^k\rangle$ where the total disappearance time $\langle\tau_d\rangle$ could be measured experimentally:

$$\langle\tau_{th}\rangle = \frac{\tau_{exp}}{p}. \tag{13}$$

I determined the correction factor $p$ empirically, both for experimental $p_{exp}$, and simulated $p_{sim}$ cases using Equation 11. In each case, the absorbing probability $p$ depends on the size of the escape window $\varepsilon$ [14]. Thus, $p(\varepsilon)$ was calculated for all analyzed escape window sizes. In the experimental case, the fraction of escaped particles were separately collected with respect to the number of all particles for each $\varepsilon$ from all 63 movies and $1/\varepsilon$ escape windows. $\overline{p}_{exp}\ (\varepsilon)$ was determined from the shape ($\beta$) and scale parameter ($\eta$) of the fit to the Weibull distribution of the collected particle fractions. According to

$$p = \eta * \Gamma\left(\frac{1}{\beta} + 1\right) \tag{14}$$

with the gamma equation Γ.

This $\overline{p}_{exp}$ $(\varepsilon)$ was then used to re-scale $\tau_{exp}$ according to the identity:

$$\tau_{exp,\,corr} = \frac{\tau_{exp}}{\overline{p}_{exp}}, \tag{15}$$

with $\tau_{exp,\,corr}$ being the corrected and $\tau_{exp}$ the measured mean first passage time, respectively. In the case of simulations with lifetime-limited traces, we found $p_{sim}$ simply from the ratio of the number of escaped particles and the total number of simulated traces.

### 2.2.11 *In silico* experiments *

*In silico* experiments were carried out with parameters ($D_{exp} = 2.29 \pm 0.05\ \mu m^2/s$, $r_{exp} = 2.44 \pm 0.13\ \mu m$) matching the *in vitro* experiments. For the simulation of trace$_i$, $D_i$ and $r_i$ were drawn independently from normal distributions. Dimensionless particles were simulated to perform a random walk in a confined domain until escape through a predefined window of size $a \pm \sigma$ on top of the domain. The spatial uncertainty $\sigma$ was derived from the *in vitro* experiments. When interacting with the boundaries of the domain, the particles were relocated to their last position before encountering the boundary. For each step, a random angle was chosen $\alpha \in [0, 2\pi]$ while the step lengths $l$ fulfilled the criterion for the probability $\rho$, Equation 16 [2]:

$$\rho^{d=2}(l,t) = \frac{2\pi}{4Dt} l\, \exp\left(-\frac{l^2}{4Dt}\right). \tag{16}$$

where $D$ was the diffusion coefficient and $t$ the time lag. Particles were counted as escaped when hitting a predefined window $a$. The time until escape, $ET$, was collected. The mean first passage time of simulated traces, $\tau_{sim}$, was determined from a fit to the exponential tail of the distribution of the collected $ET$s as described above for the experimental data.

At large relative escape windows $\varepsilon$ the time step of the simulation was chosen to be $\delta t = 10\,ms$, as in the experiment. With decreasing $\varepsilon$, the average diffusion step $\bar{l}$ became of the order of the escape opening $a$, resulting in a systematic overestimation of $\tau$. As a consequence $\delta t$ was adjusted to fulfill the criterion of $\bar{l}/a \leq 0.7$, see [77].

In simulations at very small escape openings, where the value of the spatial uncertainty $\sigma$ amounted to at least 10 % of the opening $a$ we did see that $\tau_{sim}$ seemed to level off. Similar findings were made for simulations with lifetime limitations, which were executed to test $p$. As a consequence, we conducted simulations with ideal localization precision ($\sigma = 0$) for escape openings, where $\frac{\varepsilon}{\sigma} \leq 10\%$ applied. This was the case for $\varepsilon \in [0.014, 0.011]$. At this optimized spatial resolution, flattening of the $\tau$ ($\varepsilon$) curve was prevented and the experimental observation, as well as the theoretical result, was recovered.

Simulations with and without lifetime limitations were carried out to test the performance of the correction factor. The latter was realized in simulations with extremely long trace lengths to ensure the escape of all particles ($\tau_{sim,\infty}$). To mimic the experimental situation, simulations with lifetime limitations were carried out ($\tau_{sim,p}$). This was achieved by simulation of traces with exponentially distributed lengths and a mean equal to the mean step length found *in vitro*. The resulting $\tau_{sim,p}$ was corrected as described for the microscopy data: $\tau_{sim,corr} = \tau_{sim,p}/p_{sim}$.

### 2.2.12 Statistics and error calculation *

$\tau_{th}$ was calculated according to Equation 6. In order to ensure comparability with the experimental result, $D_{exp}$ and $r_{exp}$ were used as found in the experiment - including the associated uncertainties $SE_D$ and $SE_r$. $SE_D$ and $SE_r$ were then classically propagated to achieve $SE_{\tau_{th}}$.

For the *in vitro* experiment, the total error of $\tau_{corr}$ was calculated from the sum of relative errors of the two contributing parameters ($\tau_{exp}$ and $p$ see Eq. 15) :

$$\frac{SE_{\tau_{corr}}}{\tau} = \frac{SE_{p_{exp}}}{p_{exp}} + \frac{SE_{\tau_{exp}}}{\tau}. \tag{17}$$

Since the experimental data ($\tau_{exp}$) is a result of a fit to the distribution of individual $ET$s, $SE_{\tau,exp}$ represents the standard error of the fit parameter. $p_{exp}$ and its corresponding standard error, $SE_{p,exp} = \mathrm{STD}_{p,exp}/\sqrt{N_{p,exp} - 2}$ were obtained from the mean ($p_{exp}$) and standard deviation ($\mathrm{STD}_{p,exp}$) of a Weibull distribution of all ($\mathrm{N}_{p,exp}$) collected $p_{exp}$.

$$N_{p,exp} = N_M N_\varepsilon - N_0 \tag{18}$$

depending on the number of movies $N_M$, the number of escape windows in each movie $N_\varepsilon$ ($N_\varepsilon = 1/\varepsilon$), and the number of escape sites with no registered escapes $N_0$. For the *in silico* experiments, the uncertainties in $D_{exp}$ and $r_{exp}$ were already included in the simulations. Thus, the standard error in the fit on the exponential tail of the $ET$ distribution is represented in the vertical error bar.

The error in $\varepsilon = a/(2r_{exp}\pi)$ is displayed as a horizontal error bar in the $\tau$ vs $\varepsilon$ plots. This error has two contributions, the error in the radius of the domain and the localization precision of the single emitter:

$$\frac{SE_\varepsilon}{\varepsilon} = \frac{SE_a}{a} + \frac{SE_r}{r}, \tag{19}$$

with $SE_a$ being the localization precision $\sigma$ of the single particles.

### 2.2.13 Astigmatism based single-molecule microscopy setup

The 3D SMFM setup is an extension of the existing microscopy setup as described in Section 2.2.6. The astigmatism-based 3D SMFM setup, as depicted in Figure 6, introduces a deformation of the single emitter profile using a cylindrical lens with a focal length of $f = 1\ m$. The setup is equipped with a temperature control unit, which allows measurements at different temperatures i.e., physiological conditions. A Piezo positioner was installed under the objective to allow the acquisition of a calibration curve with linked shape deformation to the axial position. With the help of this calibration curve, the position could be retrieved in subsequent data analysis. In the data analysis, a simple linear fit for the calibration curve was implemented. Building on this, optional refinements to the calibration curve such as a spline fit to the ellipticity as described in [80], and corrections for eventual refraction index mismatches [81] could be added. For this project we decided to opt for an implementation of the data analysis pipeline to the existing functions used in 2D single-molecule tracking especially since a very similar approach was already successfully applied by Holtzer [59]. In spite of a calibration curve obtained at the same optical environment under hydrogel, it was decided not to use a correction for the refraction index mismatch as described in [81].

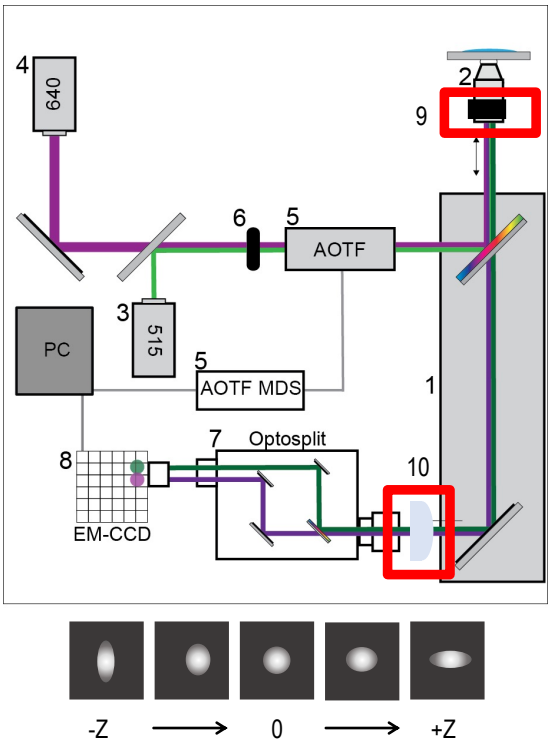


Figure 6: **Exemplary two-color 3D SMFM set-up.** The key elements of astigmatism-based microscopy are a Piezo positioner under the objective and a cylindrical lens inserted at the C-mount (marked by a red box). The sketch below illustrates the characteristic deformation of the single emitter profile as a function of the axial position. Adapted from Glogger [79].

# 3 Results

## 3.1 First attempts to create disc-shaped membrane patches

Several approaches to generate micro-patterned membranes were tested in this thesis. The first technique, based on soft lithography, built on previous work conducted during my master thesis. The base principle was to first deposit SU8, a photo-resist, on glass by spin coating. After curing the resist, various photo masks were used to prepare inverse patterns upon illumination and development of the resist. The patterns then served as a substrate for vesicle fusion which could only be successful on bare glass. This approach to prepare micro-pattered membranes with photo-resist was successfully demonstrated in my 2018 master thesis, using channel structures in the 100 $\mu m$ range. It was found that the resist provided confining and reflective properties. However, the preparation of smaller circular membrane patches in the range of 1 -10 $\mu m$ on a glass substrate remained out of reach with soft-lithography. In this study, a last attempt at the formation of distinct photo-resist micro-patterns on glass coverslips was conducted. This test was motivated by the versatility of the approach: the possibility to easily generate patterns of different geometries with soft lithography. In spite of all attempts to improve the protocol with a fresh batch of resist, reduced illumination times to prevent unspecific photo-acid buildup, or a focus on gentle development, the resolution limit of the experimental setup was not improved. Unspecific photo activation of the resist caused by scattered light or unspecific cross-linkage due to dislocated photo- acid could not be prevented. As a result, this technique was not applicable here. A clean room and hard contact of the photo mask with the resist, facilitated by vacuum in the illumination chamber, is most likely a prerequisite. Alternative approaches that were tested are vesicle rupture and membrane blotting. Despite the successful generation of giant unilamellar vesicles (GUVs), rupture of single GUVs into distinct circular patches on a glass support could not be achieved. Furthermore, a test of membrane blotting as described by Hovis [82] proved unsuccessful.

## 3.2 Establishment of a model system for systematic testing of the narrow escape problem in 2D

For systematically testing the narrow escape problem in 2D, the test system needed to be sufficiently small in order to be explored during the lifetime of the used fluorescent dye, while still matching the resolution of the microscopic method used. The preparation of a structured scaffold via soft-lithography was unsuccessful in the expected range of $5 - 15\ \mu m^2$, and other techniques tested also failed in our hands. A new approach was therefore established to meet the required scale and resolution of the experiment. Here, the structured scaffold was based on a combined colloid-metallization method as described in Section 2.2.2 and in [77]. The suitability of the new *in vitro* model system with regards to testing the narrow escape problem was evaluated by a multitude of tests.

### 3.2.1 Scaffold design

Depending on the type of colloid used as a place holder during the metal evaporation, e.g. polystyrene beads of different radii, the resulting scaffold exhibited disc-shaped holes of different sizes. A large dilution of the beads on the glass resulted in singled patterns. With increasing bead density, patterns with two or more connected holes could be generated. Figure 7 gives an example of a standard membrane patch with a radius of $\sim 2.5\ \mu m$. A high contrast of the gold scaffolding to the glass bottom of the wells in both brightfield, Figure 7 a, and fluorescence, 7 b, was observed. Single tracer lipids were tracked within the membrane patches, as depicted in Figure 7 b and c.

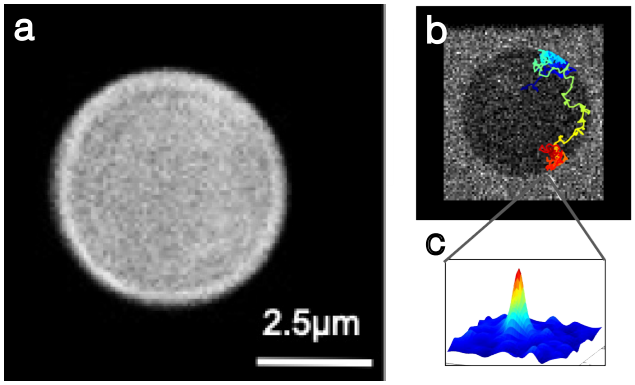


Figure 7: **Exemplary membrane patch. a** The glass bottom wells in the micro-patterned substrate appear light in contrast to the gold in brightfield microscopy. **b** The same membrane patch was imaged with single-molecule microscopy. A single emitter trace is projected onto a snapshot of the patch, with the trace is color-coded over time. **c** Gaussian fit PSF of the tracer particle in the last frame of the acquisition. The membrane patches have a radius of $\sim 2.5\,\mu m$.

### 3.2.2 The determinations of the localization precision using different methods are in agreement

The localization precision $\sigma$ of a single particle can be derived from either the standard deviation of the Gaussian fit to the PSF of the single emitter or, as described in Equation 9, from the number of detected photons. The analysis of the Gaussian fits to the ATTO647N molecules imaged in the test system resulted in $\left\langle \sigma_{exp} \right\rangle = 20\,nm$. The comprehensive approach by Thompson [52] as shown in [77] resulted in $\sigma_\gamma = 19\,nm$, which was in very good agreement with the result of the standard deviation of the Gaussian fit to the PSF.

### 3.2.3 The automated determination of the membrane patch area revealed the accuracy of the domain size

As shown in Equation 6, the theoretical mean-first passage time scales linearly with the area of the diffusion site, as seen with the membrane patch illustrated in Figure 1.

In the experimental test, the area of the membrane patches was set by the diameter of the employed colloids, here 5 $\mu m$. The actual diffusion space explored by the single particles was experimentally determined for the individual patches. To this end, a pixel mask, Figure 8c, was generated from all particle localizations in one experiment, Figure 8b. The center of mass and the radius of the pixel mask were derived.

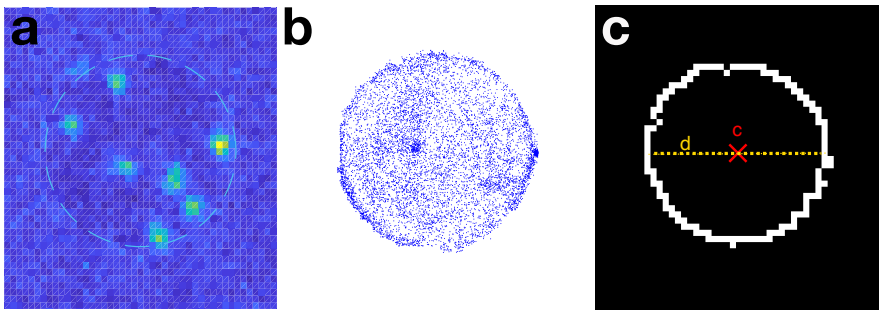


Figure 8: **The radius of the patches is determined from the localizations of the single lipids in the membrane.** **a** Exemplary snapshot of single molecules in a membrane patch. The dashed line indicates the expected boundary of the patch. It is a guide for the eye to the radius of the used colloid. **b** All single molecule localizations of mobile particles in a movie. **c** The white pixels indicate the boundary of the membrane which is included in the patch. The center of mass of the pixel mask, c, is marked in red and the diameter, d, in yellow. For the example shown here, the diameter was 30 $px = 4.8\ \mu m$. Adapted from [77].

The area of the investigated membrane patches was automatically found and the radii of all 63 membrane patches were determined from the diameter of the pixel mask. The variation in the size of the patches is illustrated in the histogram in Figure 9. The mean radius was 2.44 $\mu m$ with a standard deviation of 0.13 $\mu m$. This value was used in the theoretical calculation of the mean-first passage time and the standard deviation in the determination of the error in $\tau_{exp}$. See Figure 16 as well as Section 2.2.12.

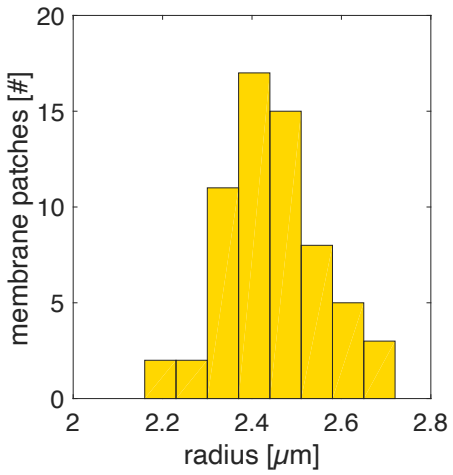


Figure 9: **Distribution of the membrane patch radii.** The distribution of the radii varied around a mean of $2.44\,\mu m$ with a standard deviation of $0.13\,\mu m$, N = 63.

### 3.2.4 Determination of the rim and center region in the membrane patches

One of the assumptions in the narrow escape problem is the presence of a reflective boundary at the rim of the diffusion domain. To judge the suitability of our novel model system, it was necessary to analyze the diffusion behavior of the tracer lipids in the rim area and in the center area of the membrane patches in order to rule out potential bias due to interactions with the gold boundary. A meaningful division of the corresponding areas had to be done, aiming for a spatial segregation with a rim region that is wide enough to harbor most 1-step diffusion events without leaving too much room for 2-step events. For technical reasons the spacial resolution was limited to the pixel size of 160 $nm$. To this end, the decision had to be made between a width of the rim of 160 $nm$ and 320 $nm$. Exemplary traces were generated by a random walk simulation mimicking the conditions in the experiment. The simulated Brownian particle exhibited a diffusion coefficient of $D = 2.29 \pm 0.05\,\mu m^2/s$ at the time resolution of the experiment: $t = 10$ $ms$. The traces were then decomposed in 1-step and 2-step events. Cumulative distributions of the corresponding step length were computed. At the chosen rim width of 2 px or 320 $nm$, 71% of all 1-steps fitted inside the rim, while only 46% of 2-steps were short enough to be included. In

comparison, a threshold of only 1 px or 160 *nm* resulted in 26% of the 1-step events being omitted, while the percentage of falsely included 2-step events decreased to 16%.

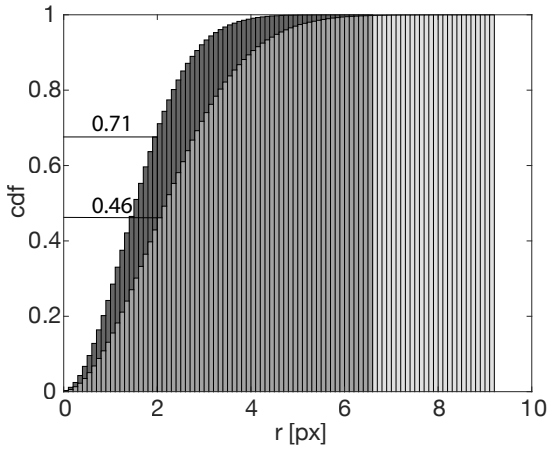


Figure 10: **Statistical comparison of random 1-step and 2-step events.** Cumulative probability of a 1-step or 2-step event (dark and light, respectively) moving a distance r in the membrane domain. The data are based on a random walk simulation employing experimental diffusion coefficients and time lags. A two-pixel travel range is indicated by the black line for the distribution of the 1 and 2-steps. Adapted from [77].

### 3.2.5 Test of membrane integrity by determination of the immobile fraction indicates a fluid membrane

A prerequisite of free diffusion on an artificial membrane is its integrity. By calculating the defect area fraction, the integrity of the membrane patches can be evaluated. To this end, particle traces were categorized into immobile and mobile tracks. Not just as an entity, but also as sub-parts of a trace. Which fraction of the surface of a membrane patch was occupied by immobile particles was investigated. The analysis was done for all 63 membrane patches, with an average of 3.6 % of the diffusion domain found to be defective with a median of 2.6 %, Figure 11.

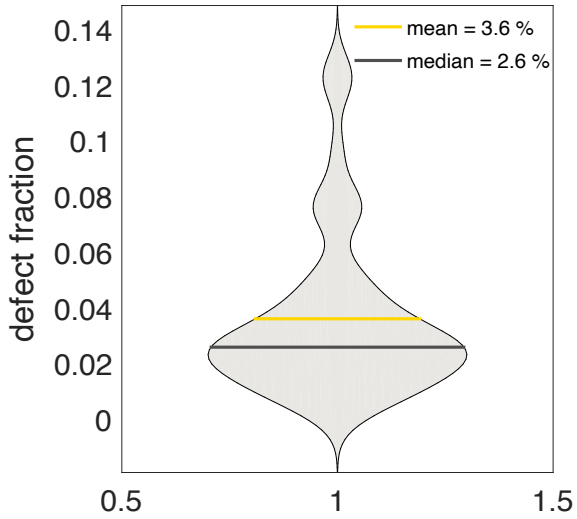


Figure 11: **Membrane quality.** The integrity of the solid supported bilayers generated to test the NEP was determined and judged by the fraction of defects. An analysis of all patches resulted in a mean fraction of defects of 3.6 %, marked in yellow, and a corresponding median of 2.6 % marked in gray. Adapted from [77].

### 3.2.6 The mean squared displacement indicates diffusive behavior of lipids in patterned membranes

According to general consensus, linear dependence of mean squared displacement over time indicates free diffusion. In the experimental analysis of the narrow escape theory, traces with a minimum length of 10 steps were selected for analysis, as described in [77]. A linear fit to the data yielded an $R^2$ of 0.98, indicating free diffusion in the model system, Figure 12. A diffusion coefficient of $D = 2.29 \pm 0.05\,\mu m^2/s$ was derived from the slope of the linear fit of the first 5 data points of the $\langle r^2(t) \rangle$ plot.

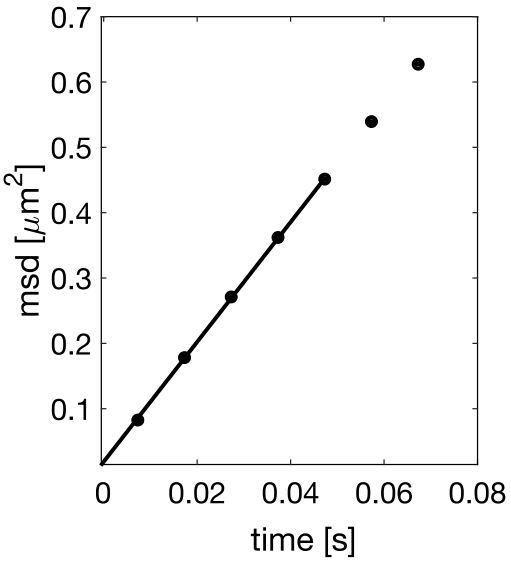


Figure 12: **Mean squared displacement analysis.** Mean squared displacement over time for all tracer lipids in the membrane patch used for the analysis of the mean first passage time. Error bars depict the standard deviation and are the same size as the markers. A linear fit to the first five data points, shown by the solid line, resulted in a diffusion coefficient of $D = 2.29 \pm 0.05\,\mu m^2/s$. Adapted from [77].

### 3.2.7 Determination of the site-specific diffusion coefficients from the distribution of 1D step lengths in the center and rim regions of the membrane patches

Based on Equation 20, a particle with a diffusion coefficient $D$ has the probability, $\rho$, of being found at the distance $l$ after time $t$, [2]:

$$\rho^{d=1}(l,t) = \frac{1}{\sqrt{4Dt}} \exp\left(-\frac{l^2}{4Dt}\right). \tag{20}$$

We can recall that free diffusion of a Brownian particle is characterized by the normal distribution of the one dimensional displacement of its movement. The distributions of 1D step lengths in the center and rim of the domain were determined and fit with a Gaussian function, Figure 13. By using the fit standard deviation, *std*, the diffusion

coefficients in the center and at the rim can be calculated as follows:

$$D_{center,rim} = \frac{std^2}{2\delta t}, \tag{21}$$

where $\delta t = 10\ ms$ was the time lag between two consecutive frames of a movie. Both fractions showed a true Gaussian distribution with $R^2$ values of $R^2 = 0.99$. Here, the width of a Gaussian fit with the corresponding data gave an indication on the diffusion coefficient. The analysis of the 1D displacements of tracers lipids in both central and rim regions of the membrane patch revealed normal distributions. However, the narrower fit on the displacements in the rim region indicated a smaller diffusion coefficient of $D_{rim} = 1.13 \pm 0.02\,\mu m^2/s$ in comparison to the center, where the diffusion was found to be almost twice as large, $D_{center} = 2.21 \pm 0.01\,\mu m^2/s$.

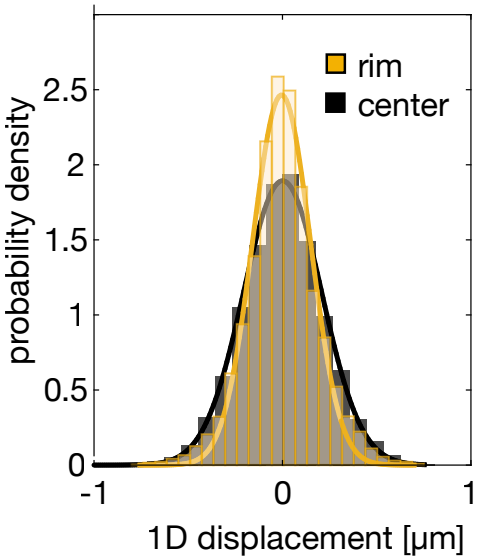


Figure 13: **1D step displacements of particle movement in the center and rim regions of the membrane patches.** Histogram illustrating the normal distribution of 1D diffusion step length of the tracer lipids in the centers (black) and rims (yellow) of the domains. Gaussian fits are depicted by the solid lines. Site specific diffusion coefficients were derived according to Equation 21 and are $D_{center} = 2.21 \pm 0.01\,\mu m^2/s$ and $D_{rim} = 1.13 \pm 0.02\,\mu m^2/s$, for the center and rim, respectively. Adapted from [77].

### 3.2.8 Evaluation of the reflective properties of the gold boundaries

The gold in the model system was chemically treated to prevent membrane formation, as described in Section 2.2.4. The localization of the tracer lipids indicated distinct membrane patches, not exceeding the boundaries. To evaluate the reflectivity of the boundaries, the angles between consecutive steps of the traces were analyzed based on the assumption that in a random walk no angle should be preferred. This analysis was performed separately for the diffusion steps in the rim and center regions (see above). A total of 282,576 and 141,564 angles were analyzed from the center and the rim. In the central region of the membrane patch, an encounter with the boundary was ruled out. A rose plot, representing all computed angles $\alpha \in [0°, 360°]$ was found to be an intuitive illustration. The angles were evenly distributed in the full range possible, both in the center and rim region. See Figure 14 for $angles_{center}$ and $angles_{rim}$, respectively.

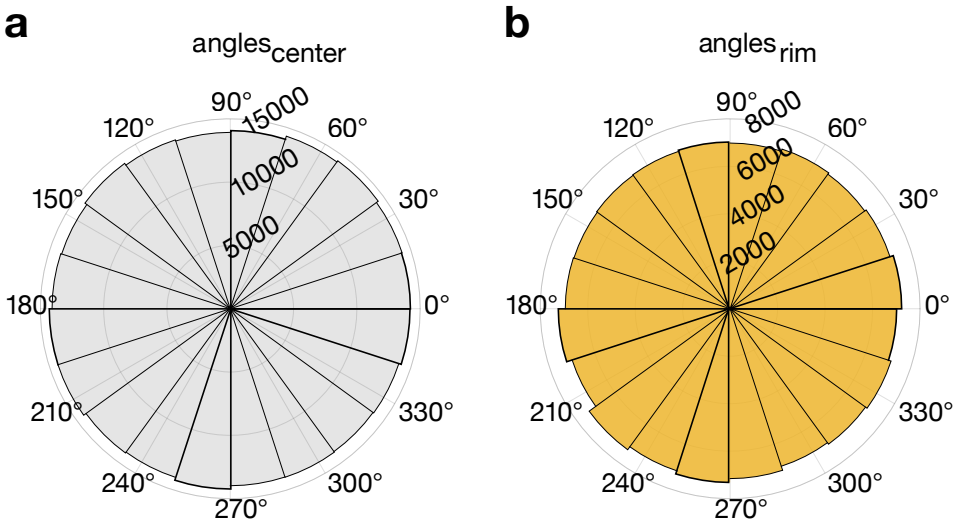


Figure 14: **Step angles in the center and at the rim region of the membrane patches.** An illustration of the angles between consecutive steps of the trajectories in the **a** center and **b** rim region of the membrane patches. All membrane patches measured are represented by the data shown. Adapted from [77].

The comparison of both distribution patterns shows no difference between $angles_{rim}$ to $angles_{center}$, indicating that the reflectivity at the rim is unbiased.

## 3.3 Experimental determination of the mean first passage time in circular model membranes

As described in the introduction and in more detail in [77], in fluorescence microscopy, single molecules cannot always be tracked continuously and infinitely. As a result, the achievable trace length is limited. For the analysis of narrow escape events this is a problem, as escape times are exponentially distributed and extremely long escape times will be underrepresented. This leads to a lack of the characteristic tail. This lifetime limitation has obstructed experimental approaches to investigate and apply the narrow escape theory.

### 3.3.1 The MFPT from lifetime-limited single-molecule traces are re-scaled by the fraction of escaped particles

The experimental mean first passage time was determined from a fit to the exponential tail of the escape time distribution. The escape site size $\varepsilon$ was varied during the analysis from fractions of the circumference of the membrane patch of $\frac{1}{8} - \frac{1}{88}$. It was observed that $\bar{\tau}_{exp}$ remained mostly constant for all tested $\varepsilon$. Table 8 lists all values.

Table 8: **The experimentally determined mean first passage time at decreasing escape opening size.** $\bar{\tau}_{exp}$ was determined from a fit to the exponential tail of the escape time distribution captured at $\varepsilon$ of different sizes. $\varepsilon$ is in fractions of the circumference of the membrane patch, $\bar{\tau}_{exp}$ in seconds.

| $\varepsilon$ | 1/8 | 1/12 | 1/16 | 1/20 | 1/24 | 1/32 | 1/44 | 1/56 | 1/72 | 1/88 |
|---|---|---|---|---|---|---|---|---|---|---|
| $\bar{\tau}_{exp}$ | 0.411 | 0.432 | 0.435 | 0.438 | 0.455 | 0.464 | 0.464 | 0.466 | 0.435 | 0.434 |

Based on the literature, the resulting $\bar{\tau}_{exp}$ was expected to increase with a decreasing window size [14]. The assumption was that all particles in the domain will escape if observed for a sufficiently long time, see Equation 11. Experimentally, it was

found that only a small fraction of particles could be tracked until their escape. Additionally, from all traces reaching the escape site only 11.73 % ± 3.60 % started from the center or farther away from the escape site and were therefore used in the determination of $\bar{\tau}_{exp}$. In order to account for the traces that cannot be traced until escape, the fraction of escaped particles, $p$, can be used as a correction factor. The applicability of $p$ is demonstrated in [77] and described in Section 2.2.10. $\bar{\tau}_{exp}$ is determined from a large dataset of escape times at various escape openings of the same size. Therefore, a mean correction factor had to be found for each escape opening size. The Weibull distribution is frequently used in reliability analyses, where the time-to-failure is calculated [83]. A Weibull with two defining parameters, shape and scale, is a powerful tool to model distributions [84]. The distribution of the collected $p$s from the openings of one size was tested for a Weibull distribution graphically in a Weibull cumulative probability distribution plot, Figure 15 a. The data follows a Weibull distribution if it agrees with a line as indicated by the yellow fit. In fact, Figure 15 a demonstrates a good agreement of the Weibull fit for exemplary data from $\varepsilon = 1\,\%$. From a fit to the Weibull distribution, Figure 15 b, the shape and scale parameter were found. Consequently, $\bar{p}_{exp}$ (1%) was determined accordingly to Equation 14 and Section 2.2.10. Figure 15 c lists the determined $\bar{p}$ for all tested $\varepsilon$. The results indicate that $\bar{p}$ decreases weakly with $\varepsilon$. All analysis was done in MATLAB.

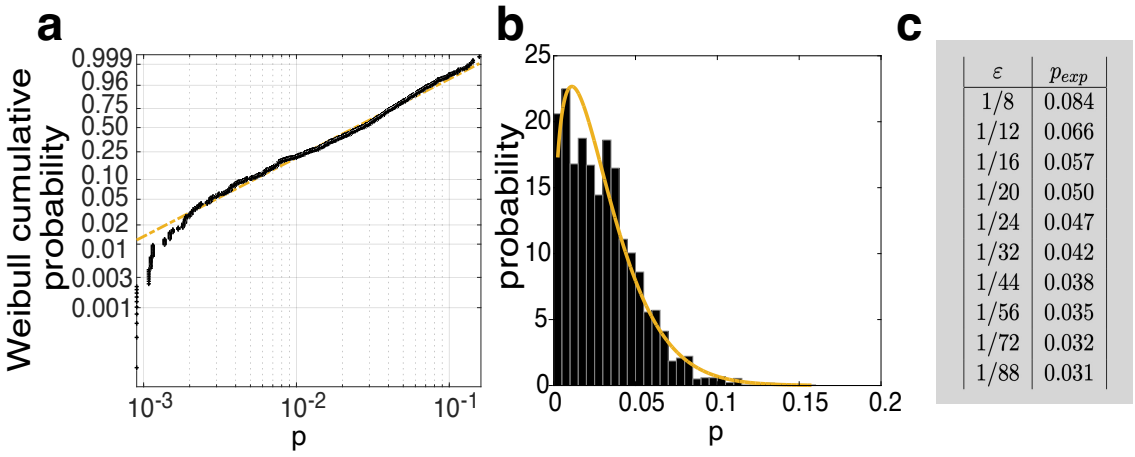


| $\varepsilon$ | $p_{exp}$ |
|---|---|
| 1/8 | 0.084 |
| 1/12 | 0.066 |
| 1/16 | 0.057 |
| 1/20 | 0.050 |
| 1/24 | 0.047 |
| 1/32 | 0.042 |
| 1/44 | 0.038 |
| 1/56 | 0.035 |
| 1/72 | 0.032 |
| 1/88 | 0.031 |

Figure 15: **The correction factor $p$. a** Plot of the Weibull cumulative probability of the correction factors $p_{1\%}$ determined from all windows of the exemplary escape opening size of 1 % (black dots). The yellow line indicates a Weibull distribution. **b** Illustration of a Weibull fit (yellow) to the $p_{1\%}$ distribution (black). **c** Table listing the correction factor $p$ for a range of escape openings $\varepsilon$. Adapted from [77].

### 3.3.2 Validation of the correction factor via systematic simulations

To thoroughly test the applicability of the introduced correction factor, $\bar{p}$, two kinds of simulations of narrow escape from a disc were conducted. Both scenarios mimicked the experimental reality with respect to the radius of the domain, the escape opening, and the time resolution.

As described in detail in Section 2.2.10 and in [77], simulations with lifetime-limited and immortal particles were conducted and compared in analog. In the ideal scenario with immortal particles, all particles would reach the escape site and $\tau$ could be determined directly from the exponential tail of the escape time distribution. This ideal result was compared to the mean first passage time from an experiment where only a fraction of the particles reached the escape site within the observation period. Due to this, the escape time distribution is insufficient, so consequently the correction factor was necessary. Thus, for the simulation with lifetime-limited particle traces, correction factors were deduced and the mean first passage time was

corrected. The corrected times were subsequently compared with results from immortal particles. It was found that the correction factor was able to re-scale the limited results, matching the results from immortal traces, which did not need correction. Table 9 lists the values for the mean first passage time from simulations with immortal particles, $\bar{\tau}_{sim,\infty}$, and from life-time limited traces, $\bar{\tau}_{sim,corr}$ for all tested $\varepsilon$.

Table 9: **Comparison of $\bar{\tau}_{sim}$ from lifetime-limited and immortal particles.** The table lists the relative escape opening, $\bar{\tau}_{sim,\infty}$ from simulations with infinite particle lifetime and $\bar{\tau}_{sim,corr}$ from simulations with lifetime-limited particles. Asterisks indicate values from simulations with a localization precision of $\sigma = 0$. All units of $\bar{\tau}$ are in seconds $[s]$. Adapted from [77].

| $\varepsilon$ | $\bar{\tau}_{sim,\infty}$ | $\bar{\tau}_{sim,corr}$ |
|---|---|---|
| 1/8 | 5.66 | 4.68 |
| 1/12 | 7.12 | 6.17 |
| 1/16 | 8.40 | 8.19 |
| 1/20 | 9.15 | 9.85 |
| 1/24 | 9.87 | 9.96 |
| 1/32 | 12.00 | 12.05 |
| 1/44 | 11.49 | 11.86 |
| 1/56 | 12.94 | 13.33 |
| 1/72 | 13.78*,12.73 | 13.06 |
| 1/88 | 14.26*,12.88 | 13.15 |

### 3.3.3 The experimental determination of the mean first passage time agrees with the theoretical prediction.

After the successful introduction of the correction factors, the stage was set to apply the same kind of correction to the experimental data. $\tau_{exp}$ was re-scaled with $p$ (see Section 3.3.1) and the resulting $\tau_{exp,corr}$ was compared with the theoretical prediction $\tau_{th}$ of $\tau \propto \ln(1/\varepsilon)$.

Figure 16 illustrates the dependency of the mean first passage time on the escape opening size $\varepsilon$. For small $\varepsilon \in [1.1\,\%, 5\,\%]$ the values for $\tau_{exp,corr}$ were in very good agreement with $\tau_{th}$. As the escape site size exceeded 5 % of the circumference, the results diverged. The results indicate that $\tau_{exp,corr}$ follows $\tau \propto \ln(1/\varepsilon)$ in the limit of small escape openings. The depicted error bars result from a combination of individual errors and are described in detail in Section 2.2.12 and [77].

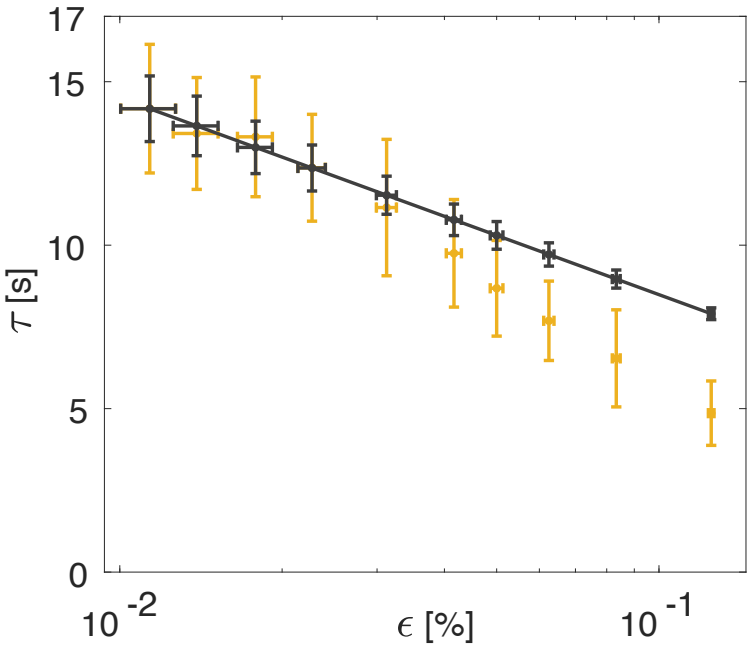


Figure 16: **Comparison of the experimentally determined and theoretically predicted impact of the escape opening on mean first passage time.** The mean first passage time from lifetime-corrected experimental data $\tau_{corr,\,exp}$ (yellow) and theory, $\tau_{th}$ (black), as a function of the escape opening $\varepsilon$ is depicted. The solid black line indicates the trend in $\tau_{th}$ as a guideline to the eye. The vertical error bars in the theory display the combined error in $r$ and $D$ whereas for $\tau_{corr,\,exp}$ the vertical error is a combination of the absolute standard error of the fit to the $ET$s and $p$s. Horizontal errors represent the absolute standard error of $\varepsilon$, applicable for both data sets. Errors were calculated as described in the Section 2.2.12. Adapted from [77]

From the literature we know that the escape times are exponentially distributed [16]. Experimentally, the mean first passage time is derived from an exponential fit

on individual escape times of Brownian particles in a disc. Figure 2 illustrates an exemplary trace of a Brownian particle diffusing in a circular domain and escaping through a small opening at the top the confinement.

## 3.4 Experiment-inspired simulations

The random walk simulations used to test the correction factor were, as mentioned above, inspired by the experiment. A correct determination of the mean first passage time requires exponentially distributed escape times [16]. The simulations met this prerequisite. As shown, $\tau_{sim,\infty}$ and $\tau_{sim,corr}$ delivered comparable results for the mean first passage time. The $\tau_{sim,\infty}$ was less desirable technically, due to long computing times. Therefore, all following simulations were done with lifetime-limited particles and always checked for the exponential distribution of the escape times, unless otherwise stated.

### 3.4.1 Simulations of NEP in 2D support the *in vitro* findings

The *in vitro* and *in silico* experiments were compared in an attempt to do a comprehensive analysis of the narrow escape problem in a disc. Where applicable, the *in silico* results were taken from the simulations already run for the $\tau_{sim_{corr}}/\tau_{sim_{\infty}}$ experiment. Figure 17 shows the results of the *in vitro* experiment in yellow, alongside those of the *in silico* experiments ($sim_{\infty}$) in green. The results show agreement across the entire spectrum of escape openings studied. The agreement explicitly included the rage of $\varepsilon > 5$ % where the theoretical curve started to deviate. The simulations for the two most narrow $\varepsilon$, however, were still within the error margins of the experiment, and seemed to level off. Every localization within a margin of $\sigma = 20\,nm$ around the escape site was counted as escaped in the analysis. In these cases where a leveling effect is visible, the localization precision accounts for more than 10 % of the escape opening width. To exclude this uncertainty, these experiments were repeated with a localization precision of $\sigma = 0\,nm$, indicated with markers in light green in Figure 17. The leveling effect was found to be eliminated in simulations with $\sigma = 0$.

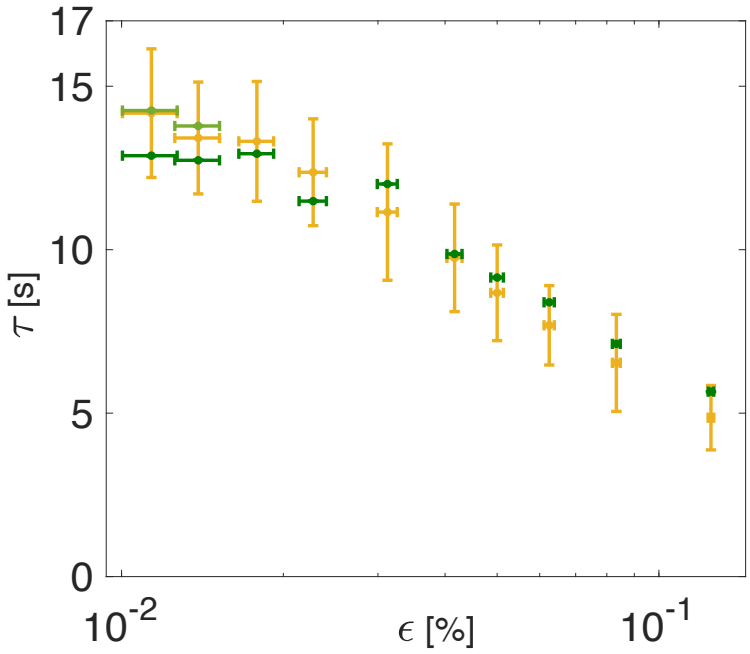


Figure 17: **Random walk simulation and *in vitro* experiment results support each other.** Mean first passage times from random walk simulations, $\tau_{sim,\infty}$, green, and experimental data, yellow, $\tau_{corr,exp}$ as a function of the escape opening $\varepsilon$. Simulations with a localization precision of $\sigma = 0$ are shown in light green. Adapted from [77]

The ability to use random walk simulations to represent the experimental situation accurately opened the door to investigate other aspects of the theory, for which the statistics used were no longer sufficient.

### 3.4.2 When does the mean first passage time become statistically independent?

In the analysis of the random walk simulations, the reliability of $\tau_{sim,corr}$ depends on the sufficiency of the statistics. The influence of increasing statistics was investigated in an experiment. 1300 escape times resulting from an example simulation ($radius_{area} = 1\ \mu m$, $D = 1\ \mu m^2/s$, $\varepsilon = 1\%$) were divided into sets with increasing size. With 800 or more escape times contributing, the simulation result converges. We now know that $\tau_{sim,corr}$ becomes more robust when the statistics of escape times

increases to at least 800 or more escape times. Based on this result, further *in silico* experiments were designed.

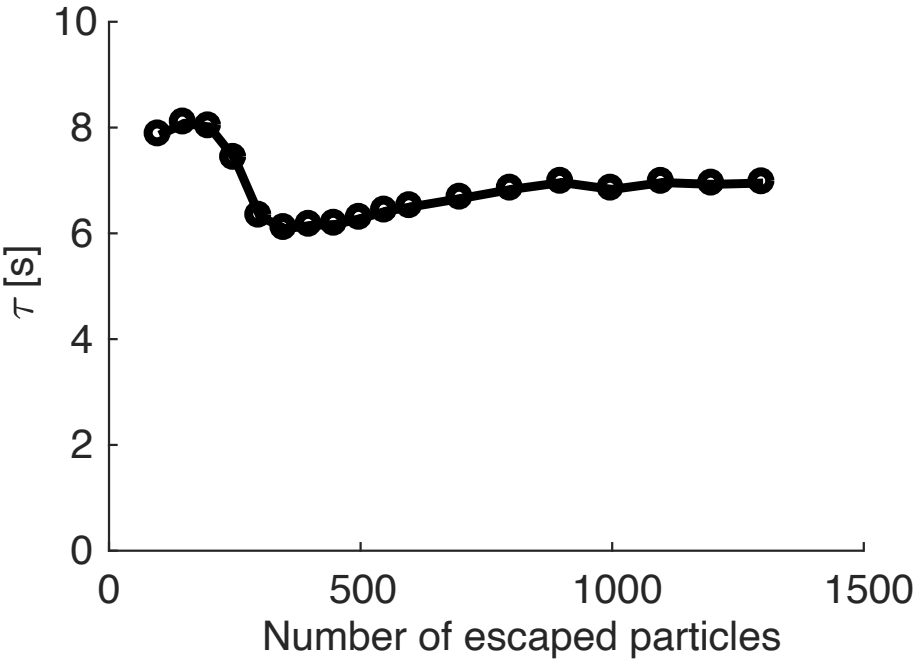


Figure 18: **The robust determination of the mean first passage time is ensured with sufficient statistics in the escape time distribution.** The displayed values for $\tau$ (black dots) are derived from one dataset of an exemplary simulation ($radius_{area} = 1\,\mu m$, $D = 1\,\mu m^2/s$, $\varepsilon = 1\,\%$) including varying amounts of particle traces. The line was added as a guide to the eye.

### 3.4.3 Distance-dependence of the mean first passage time

Theoretical considerations by Holcman et al. showed that the extent of the separation of the particles from the escape site at the beginning of the movement influences the mean first passage time. However, the effect is stated to be only true for small distances from the escape site $a$ [8]. If the particles started at least from the middle of the domain the mean first passage time is should be independent [8]. In order to test this theoretical prediction, I ran simulations of immortal particles starting at increasing distances from the escape site. Simulations with different values for $\varepsilon$ were analyzed, $\varepsilon = 1\,\%$ and $5\,\%$. The results showed a strong, almost linear, increase of $\tau$ with the decreasing start distance. The increase slowed down at $3\mu m$ of the

escape site, and the mean first passage time was saturated with distances around $4\mu m$ of the escape site. The effects were found for results of both tested escape opening sizes. Figure 19 illustrates the findings for a diffusion domain of $radius_{area}$ $= 2.5\,\mu m$ with particles diffusing at $D = 1\,\mu m^2/s$. The theoretically determined mean first passage time was 28.8 s and 18.7 s for $\varepsilon = 1\,\%$ and $5\,\%$, respectively. The number of escape times contributing to a data point varied from 280 to 663 and 393 to 882 for $\varepsilon = 1\,\%$ and $5\,\%$, with smaller contributions for larger start distances.

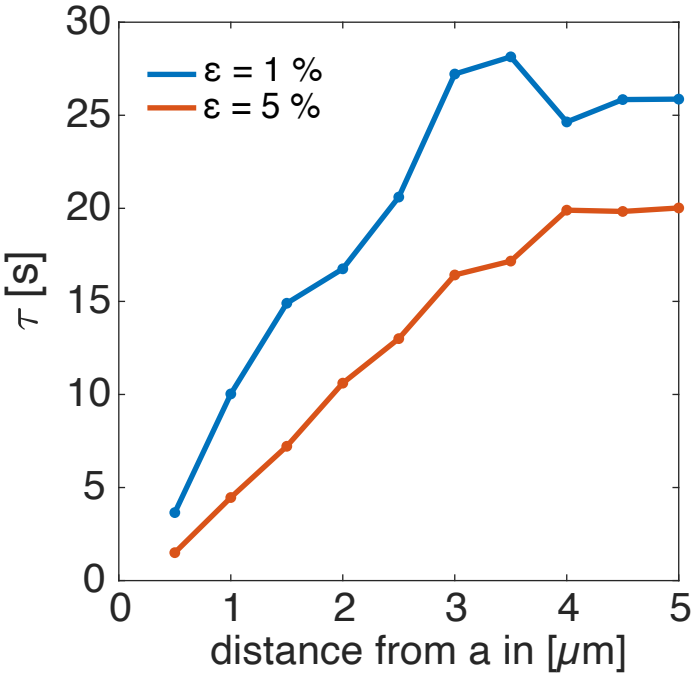


Figure 19: **The mean first passage time in relation to the start distance.** Values for $\tau$ as a function of the start distance from the escape site were derived from random walk simulations with immortal particles. The size of the diffusion domain and the diffusion coefficient of the particles was $radius_{area} = 2.5\ \mu m$ and $D = 1\ \mu m^2/s$. Markers in blue and red represent simulations with $\varepsilon = 1\%$ and $5\%$, respectively. The lines are guidelines to the eye.

A linear dependence of $\tau$ on start distance was observed for distances less than $radius_{domain}$. The data did not indicate an independence of the mean first passage time from the start distance after a threshold of one radius of the enclosing domain, but a larger threshold. However, the limited statistics prevent a clear statement.

### 3.4.4 Is the mean first passage time affected by the location of the start points in the simulation

As the mean first passage time appeared to be independent of the distance to the escape site if the particles started at a certain threshold apart, it was important to investigate the influence of the start coordinates. In this *in silico* experiment, two datasets were generated by random walk simulations which differed in the start coordinates of the particles. In one simulation the particles started in the center of the domain, $radius_{area} = 2.48\,\mu m$. In the second dataset, the particles started on random points along a line beginning at the center of the domain and reaching the outer rim of the disc, opposite to the site of the escape opening. The start distances on this line were taken from a pool of possible distances derived from corresponding *in vitro* experiments. Figure 20 shows the dependency of $\tau$ on the escape site size $\varepsilon$ for the described simulation scenarios. The results agree well.

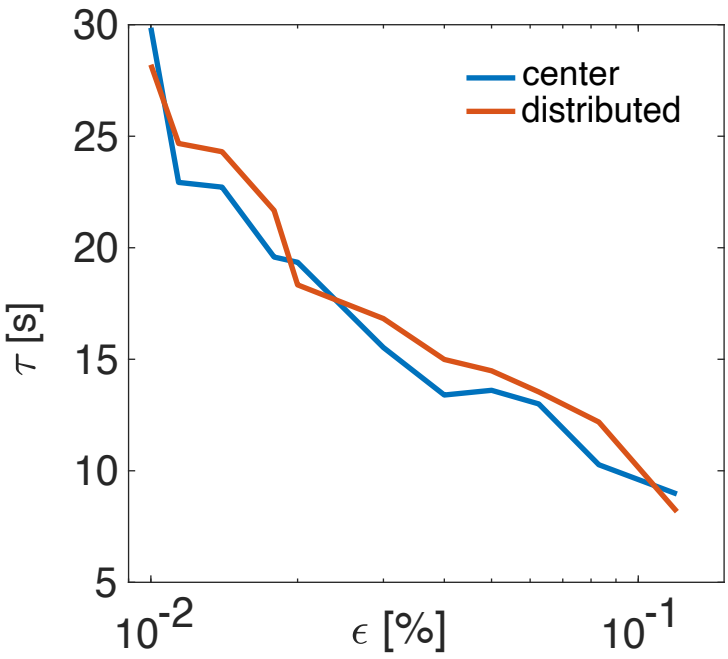


Figure 20: **The dependency of the mean first passage time on the starting coordinate of the particle.** The displayed values for $\tau$ are derived from simulations with the parameters: $radius_{area} = 2.48\,\mu m$, $D = 1.52\,\mu m^2/s$, $\varepsilon = 1 - 12\,\%$, differing in the start point of the particles. Results from particles starting in the center of the domain or on locations derived from the experiment are depicted in blue and red, respectively.

## 3.5 Establishment of the astigmatism-based 3D SMFM extension to measure in *T.brucei* cells

In this part of the Ph.D. project, I started to establish a three dimensional single-molecule fluorescence microscopy (3D SMFM) extension to an existing single-molecule microscopy setup and data processing pipeline. The establishment of the necessary hardware was completed within this project, whereas the complete integration of the data processing and the evaluation are still ongoing.

### 3.5.1 Technical realization

The hardware for the 3D SMFM extension included the P-721.SL2 PIFOC Piezo z-stage (PI), the corresponding E-709 Digital Piezo Controller (PI) the N-BK7 plano-convex cylindrical lens (Thorlabs), and an alternative C-mount side port coupling with integrated rotatable lens holder (Cairin). I installed all parts and implemented the Piezo control unit to be accessible via the $\mu$-Manager software. The C-mount harbors the plano-convex cylindrical lens and is installed between the microscope and the optosplit. By insertion of the lens here, a point-spread function (PSF) deformation was imposed on the emission light. The commercially available C-mount allowed the rotation of the mounted lens during imaging, which provides easy alignment of the deformation axes to the camera chip grid. To deform signals in the channels ($640\,nm$) and ($515\,nm$) separately, plano-convex cylindrical lenses can be inserted directly into the optosplit, where the emission light is collimated. The custom mounts (University workshop) do not allow adjustment of the lens orientation, however. In this thesis, all experiments were conducted with the plano-convex cylindrical lens in the commercial C-mount.

#### 3.5.1.1 Astigmatic deformation of the point spread function

The astigmatism inflicted by a plano-convex cylindrical lens, $f = 1\ m$, in the emission beam path introduces two foci with the circle of least confusion or medial focus in the middle. Figure 21 illustrates the deformation of the point spread function (PSF) of multifluorescent beads as an example. A series of 2000 images was taken

in crop mode with continuous illumination. The multifluorescent beads were illuminated for 9 $ms$ with a 640 $nm$ laser at an intensity of 1 $mW/cm^2$. Consecutive images were taken while manually traveling from 1 $\mu m$ below the medial focus to 1 $\mu m$ above. The cylindrical lens introducing the astigmatism was positioned so the direction of the elliptical deformation of the PSF was aligned to the horizontal and vertical axis of the camera chip.

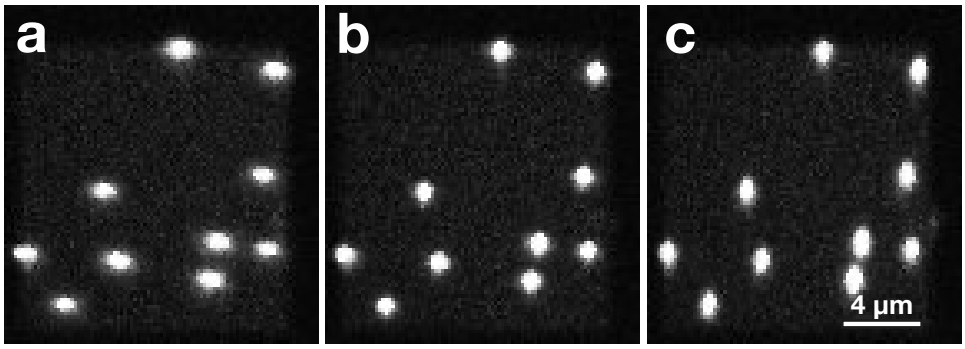


Figure 21: **Astigmatic deformation of the PSF.** Multi-fluorescent beads were imaged along the axial plane. **a** 1 $\mu m$ below the focal plane, **b** at the circle of least confusion, which is also called the medial focus and lies in between the sagittal and the tangential focus and **c** the deformation of the PSF 1 $\mu m$ above the medial focus.

The astigmatic deformation can be quantified by the change in the ellipticity, $e$ of the PSF. Here, an elliptical Gaussian was used to fit the single emitter profiles and calculate $e$. An astigmatism-based microscope encodes axial position with ellipticity, as Figure 21 demonstrates. The change of $e$ can be linked to the movement of the microscope stage. With a Piezo positioner, at the stage or the objective, axial displacements on the $nm$-scale are possible. The latter was used to move the image of the bead sample along the z-axis. In this example the objective was moved with a step size of 10 $nm$. The single molecule positions (x,y,z) deduced with the elliptical Gaussian were separated for their relative error to not exceed 0.3. A plot of single emitter positions of 7 multi-fluorescent beads along the axial image plane is shown in Figure 22. Blue markers indicate positions with a relative error in x,y, or z less or equal than 0.3, and red markers positions with a relative error in x,y, or z higher than 0.3. As expected, the criteria of a too large error (indicating a low resolution of the position) was almost exclusively met in the z coordinate. Here, the mean

absolute error was found to be 30 $nm$. The x and y coordinates were found to be more reliable, with a mean absolute error of 17 $nm$.

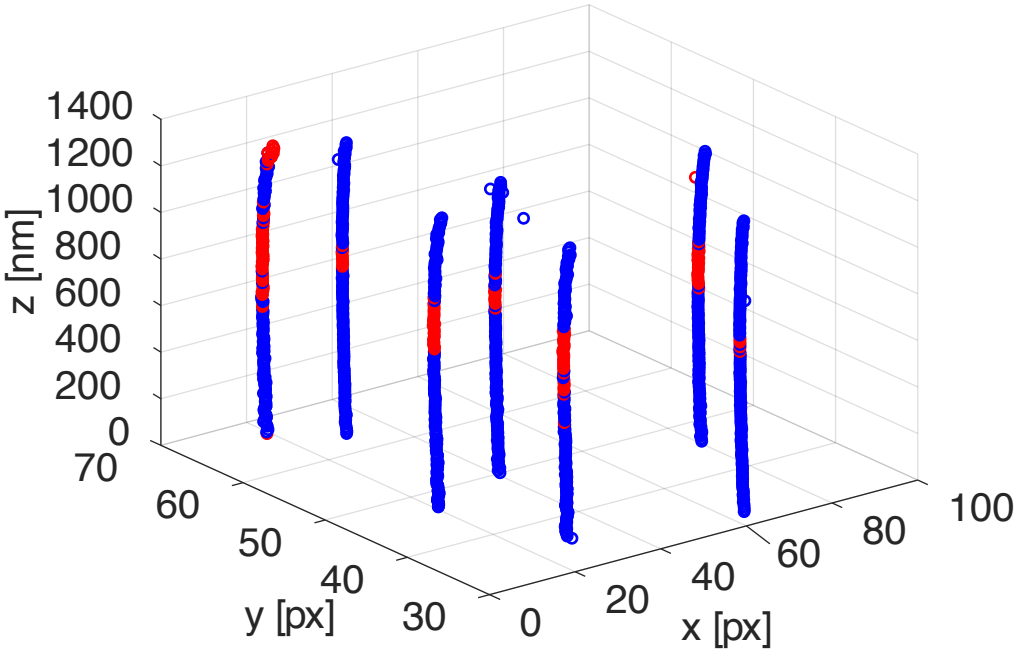


Figure 22: **Multi-fluorescent beads imaged along the axial plane.** Localization of seven exemplary beads over a travel range of 1400 $nm$ with a step size of 10 $nm$. Blue markers indicate data with a relative localization error of less than 0.3, red markers indicate higher relative errors.

#### 3.5.1.2 Calibration curve with automated linear fit

A look-up table allows the calculation of the z-position of a single molecule from the corresponding ellipticity. The first straightforward approach to generate a look-up table is to use the linear regime of the ellipticity. A Piezo-positioner was used to automatically image the signal deformation of multi-fluorescent beads along the z-axis. In the following example, a sample with beads in a hydrogel on glass coverslips was imaged. A total of 12 stacks with multiple beads each were recorded. The deformation was determined with an elliptical fit to the emitter profiles. For individual particles, the value with the least elliptical deformation was found in each deformation curve and set to zero. All curves were aligned automatically via this reference point. One average calibration curve was calculated per stack. Subsequently, the deformation curves from 12 individual movies were fitted to generate

the final calibration curve.

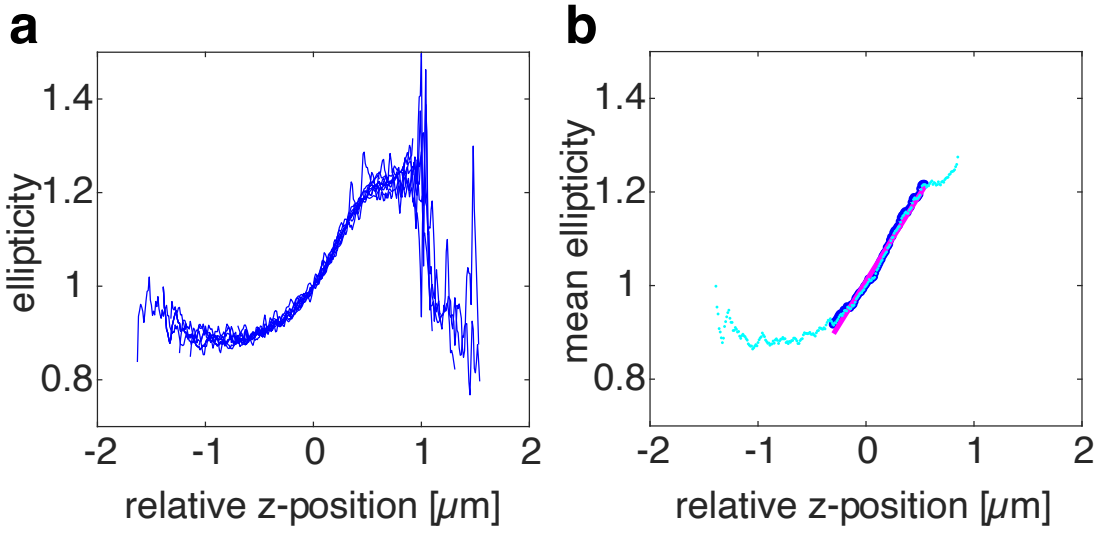


Figure 23: **Calculation of a look-up table from the linear regime of the calibration curve.** Multi-fluorescent beads were imaged with the 3D SMFM setup and the 640 $nm$ laser line in an axial range of 2 $\mu m$. **a** Each individual line plot represents the average ellipticity $e$ of one of the 12 bead samples. Each sample contained multiple beads. **b** Cyan markers indicate the mean ellipticity of all signals found at a given z position. The linear regime of the mean ellipticity data is marked in dark blue. The pink line is a fit to the linear regime. All datasets are aligned to the medial focus corresponding to z = 0.

#### 3.5.1.3 The calibration curve determined from different labels.

I compared the calibration curve obtained from ATTO647N and multi-fluorescent beads. Both emitters were embedded in a hydrogel and imaged with the 3D SMFM setup and the 640 $nm$ laser line. The Atto dye was chosen as being representative of a common dye for single-molecule microscopy, whereas the multi-fluorescent beads were chosen as an example of an ideal emitter with regards to brightness and photostability. Future applications of the 3D SMFM setup are planned to involve experiments with live *T.brucei* cells, which require embedding in a hydrogel. From the literature we know that the refractive index mismatch of the sample and the buffer can introduce an aberration of the z-distance [60, 85]. For now, we assume

that the refractive index of the hydrogel is comparable to the value for water at 25 °C and $\lambda = 647\ nm \sim 1.33$. As a consequence, both emitters were embedded in hydrogel to match future experiments in living cells. The calibration curves in Figure 24 were the result of 34 and 12 stacks of multi-fluorescent beads and ATTO 647N molecules, respectively. The ellipticity was measured and aligned as described in Paragraph 3.5.1.2. The measured ellipticity from all molecules in one frame was averaged and is depicted as a dot in the corresponding color for multi-fluorescent beads and ATTO 647N. All stacks were analyzed to determine the mean ellipticity corresponding to a relative z-position. Less variation was found in the individual data points derived from the beads, whereas the example of ATTO 647N resulted in a higher variation of ellipticity at a given relative z-position. The calibration curve of the multi-fluorescent beads was applicable over a wider range than the one of the ATTO 647N molecules. The linear regime spanned approximately $0.6\,\mu m$ and $0.3\,\mu m$, respectively.

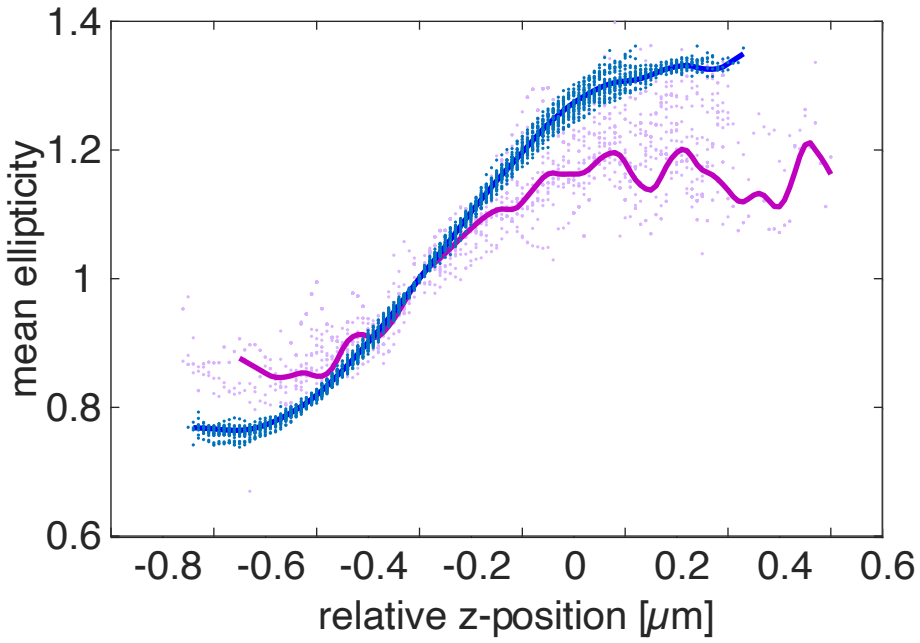


Figure 24: **Calibration curves for multifluorecent beads and ATTO 647N in a hydrogel.** Multi-fluorescent beads and ATTO 647N in a hydrogel were imaged with the 3D SMFM setup and the 640 *nm* laser line at increasing axial positions. The mean ellipticity was determined from all particles in one frame. Values for multi-fluorescent beads are depicted with blue dots and ATTO 647N molecules with magenta dots. Solid lines in the corresponding colors represent the mean over the imaged samples.

### 3.5.2 Preliminary results

The establishment of the 3D SMFM was done with a particular application in mind, namely an interesting narrow escape scenario in *Trypanosoma brucei*. It concerns the variant surface glycoprotein (VSG) dynamics on the cell surface, which are terminated by endocytosis only at the narrow flagellar pocket. Trypanosomes are single-celled parasites and cause sleeping sickness in people and nagana in livestock. Besides their obvious relevance to infection biology, they are also an excellent model system to address fundamental questions in various fields of biology. As part of their strategy to evade the host's immune response and maintain parasitemia, they undergo a constant exchange of their very dense surface coat with an intracellular pool. In *Trypanosoma brucei* endo- and exocytosis occurs solely at a small plasma membrane invagination called the flagellar pocket. After internalization at the flagellar pocket, endocytic vesicles become part of the endomembrane system and are trafficked to the lysosome. Vesicular traffic is therefore of utmost importance both for the parasite population to evade the host's immune system, and for parasite nutrition. The curvature of the cell surface, the flagellar pocket, and the endomembrane system in general makes a 3D approach necessary to study the dynamics of these surfaces.

To date, the setup of the 3D SMFM has not been completed. Further testing and improvements to achieve the high spatiotemporal resolution needed to track the fast dynamics of the surface VSGs are still required. Another interesting subject that is coming into focus at a research group I am associated with is the localization and dynamics of the motor protein myosin 1 (Tb927.4.3380) in *T.brucei*. Myosins are a conserved superfamily of motor proteins, which use actin as a track and have multiple roles in endocytic and endomembrane trafficking throughout the eukaryotes. The characterization of the myosin proteins in *T.brucei* is still very preliminary. As of today, we only know that the depletion of myosin I leads to a termination in the vesicular traffic from the flagellar pocket. Therefore, it was concluded that endocytic vesicular uptake is myosin-dependent in *T. brucei* [86]. So far, nothing is known about the behavior of the trypanosome myosins at the single-molecule level. Super-resolution microscopy seems to be the ideal technique to investigate the localization and dynamics of the myosins.

In order to image myosin 1 on the single molecule level, I established a stably-transfected cell line expressing HaloTag-TbMyo1. The required HaloTag-TbMyo1 construct was generated by *in vivo* assembly. With the introduced HaloTag labeling system various dyes can be linked to the protein of interest. First tests with the cell-permeable Janelia Fluor-JF646 (quantum yield $\Phi = 0.54$, extinction coefficient $\epsilon_{max} = 152,000\ M^{-}1\ cm^{-}1$) [87] dye yielded promising results. In the following, I would like to include some preliminary data to illustrate the status of the Halo labeling in our hands. So far, the imaging was conducted with the wide-field single-molecule microscope which was described earlier in this thesis. Thus far the cylindrical lens was not inserted at the time of acquisition, therefore 2D images and movies were captured. The localization of a HaloTag-TbMyo1 in the cell body, derived from labeling with the JF646 Halo ligand, was found to be consistent with the myosin localisation patterns observed in a cell line expressing TbMyo1 coupled to the fluorescent protein mNeonGreen (mNG) and also the endogenous TbMyo1 protein. In all cases, TbMyo1 was found predominantly in distinct spots in the posterior end of the cell (Figure 25).

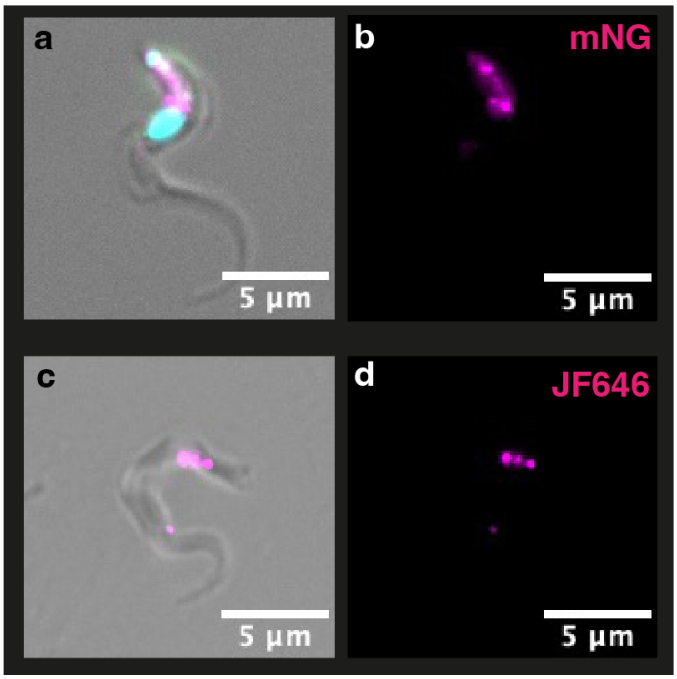


Figure 25: **The localization of TbMyo1 in *T.brucei* cells.** TbMyo1 was visualized with two different tags to detect the localization pattern of myosin in *T.brucei* cells via fluorescence microscopy. **a** Fixed mNG-TbMyo1 cells show the localization of mNG-TbMyo 1 (magenta) between the kinetoplast and the nucleus (cyan). **b** mNG-TbMyo1 signal only. **c** HaloTag-TbMyo1 cells were stained with the Halo-ligand JF646 (magenta). HaloTag-TbMyo1 localized near the posterior end of the cell. **d** JF646 signal only. **a,b** courtesy of the Morriswood group, Sisco Jung.

Single-molecule tracking experiments on HaloTag-TbMyo1 cells (n = 39) in 2D have given a preliminary impression of the dynamics of the myosin motor protein and on the performance of the JF646 Halo ligand. The distribution of the single molecule traces was similar to the findings from lower resolution imaging, as in Figure 25. The detected single-molecule traces of TbMyo1 seemed to localize within a larger area of the cell body, but most of the signal was detected in the posterior end of the cell. An exemplary micrograph, Figure 26 shows a projection of all traces with more than 10 consecutive steps color-coded by time over the total acquisition time of 50 $s$. A preliminary analysis of $\sim$ 700 traces yielded an average molecule track length of 27 frames (0.27 s). A wide range of diffusion coefficients (0.10-3.60 $\mu m^2/s$) with a modulus of 0.037 $\mu m^2/s$ were detected. These test data on the cell line were

conducted with TrackIt [88].

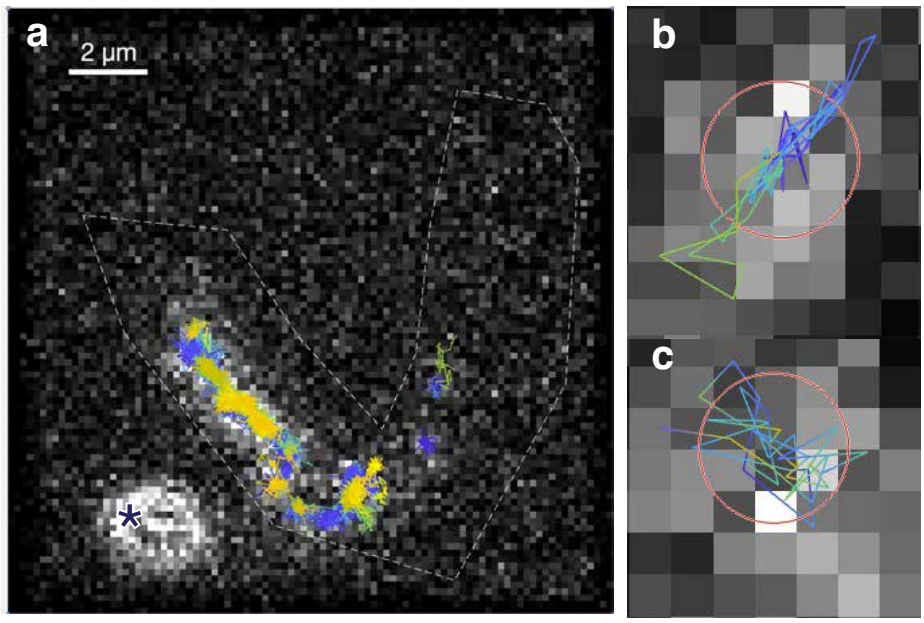


Figure 26: **Example of single-molecule traces of HaloTag-TbMyo1 in living *T.brucei* cells labeled with JF646.** Individual HaloTag-TbMyo1 molecules were localized via a Gaussian fit and tracked with a nearest-neighbor analysis. **a** All 779 traces found in 5000 consecutive movie frames are plotted with a color code according to time. The dashed line represents the region of interest in which the localization and tracking were performed and roughly marks the outline of the cell, with the posterior end of the cell pointing to the top left of the image. An asterisk marks the position of a multi-fluorescent bead. **b,c** Exemplary traces of single TbMyo1 molecules labeled with JF646 via the Halo tag, taken from **a** the mean track position is marked with a red circle. Cells were immobilized in a hydrogel.

The first attempts at 3D imaging did not result in meaningful single molecule tracking, but suggest a possible total imaging depth of 300-600 $nm$ with an axial resolution, $\sigma_z$, of 120 $nm$ and a lateral resolution, $\sigma_{x,y}$, of 26 $nm$ at a temporal resolution of 10 $ms$ to be expected in the future.

# 4 Discussion

In this thesis, I established a novel model system to systematically test the narrow escape problem in a disc. This model system was thoroughly characterized and evaluated. In Section 4.1 I will discuss the individual features of the characterization and their importance for the application, as well as potential weaknesses and uncertainties. Furthermore, in Section 4.2, I will review the results of the systematic, experimental test of the narrow escape problem in a disc with particular reference to the theoretical prediction of the mean first passage time. The experimental test of the mean first passage time was complemented with matching random walk simulations. The latter were used to investigate several questions regarding the experimental approach and the theory. Besides the comparison to the experimental and theoretical result of the mean first passage time, the legitimization of the correction factor, and the influence of the start distance of the particles from the escape opening, as well as the importance of sufficient statistics will be evaluated in Section 4.3. A minor part of this thesis was to establish a 3D SMFM extension. Section 4.4 evaluates the status of that project and addresses possible enhancement.

## 4.1 Establishment of a novel model system for systematic testing of the narrow escape problem

In this study, the aim was to establish a test system for the narrow escape theory in 2D. The model system I developed is based on a combination of colloid metallization and vesicle fusion. This model system allows imaging with the custom inverted microscopy setup and builds on existing in-house expertise in SLB formation. The results of the evaluation process of this model system indicate that it is suited to reliably test the narrow escape problem in a disc.

Overall, the colloid-metallization approach proved to be a relatively simple and efficient method of preparing scaffolds, which can also be used in high-throughput applications and have a long shelf life. However, the structures are not reusable, as cleaning attempts with plasma or detergents lead to damage to the gold coating, whereas ethanol and water rinses alone were insufficient in restoring the clean, hydrophilic properties of the glass. With regards to imaging, the utility was supported by the fact that due to the high contrast of the bare glass and the gold scaffold the area of interest was easy to localize using both bright-field and fluorescence microscopy. Gold, among other precious metals, is reported to quench a fluorescent signal if near the fluorescent emitter [89]. This carries the risk of variation in the signal intensity at different loci of the diffusion domain. In contrast, the long aliphatic chains of the 1-dodecanethiol, which was used to functionalize the gold, should be sufficient to separate the tracer lipids from the gold boundary. The quenching of the fluorescence intensity as well as a reduction of the fluorescence lifetime for a fluorophore is reported to to be most prevalent within short distances to the gold. The effect becomes less with distances smaller than $15\,nm$ and not recognizable at around $30\,nm$ [90]. To investigate the hypothesis of a reduced signal near to the gold boundary, a comparison of signal intensity close to the gold boundary and in the rest of the domain was conducted. A quenching effect was not seen, however. The stated advantages stand in contrast to the previously tested soft lithography approach, which could not offer any of these benefits in our hands.

The quality of the single-molecule microscopy data obtained in the new model system was evaluated. The localization precision of the single particles was found to be $\sigma = 20\ nm$. This high spatial resolution lies at the lower end of the typical range

for single-molecule localization microscopy [23, 48].

The mean signal-to-noise ratio was found to be 115 with a standard deviation of 35. This is considered to be a good value for this microscopy method. The comparison to earlier studies in unpatterned solid-supported lipid bilayers of comparable composition where Schmidt for example achieved values of $SNR = 28$ strongly supports this assumption [23].

An important parameter in the systematic test of the narrow escape problem is the area of the diffusion domain. In the introduced model system, this domain is represented by the membrane patches inside the micro-structured scaffold. The colloids used to create the scaffold had a radius of 2.5 $\mu m$. The analysis of the membrane patches revealed a narrow variation in the radii of the generated model membranes of 2.44 $\mu m$ with a standard deviation of 0.13 $\mu m$. A small patch size error supports comparison of individual patches, minimizing the error in the resulting mean first passage time. Due to a lack of insight into the error in the colloid diameter, its impact on the final membrane patch radius cannot be singled-out.

A fluid membrane is a prerequisite for free diffusion within a model membrane. The preparation of solid-supported lipid bilayers harbors the possibility of defects, most likely caused by interactions with the glass support as a result of a insufficient physicochemical state [91]. The introduced defects in the lower leaflet can be transmitted to the upper leaflet by inter-leaflet coupling. In this study, only lipids in the upper leaflet were measured, potentially reducing the effect of defects from the substrate. Extensive chemical and physical cleaning of the substrate prior to membrane introduction by vesicle fusion is also known to reduce defects and was therefore performed. In addition, this treatment introduces the paramount hydrophilicity necessary to facilitate membrane formation on a thin layer of water molecules [92, 93]. In general, surface defects can be assessed directly by atomic force microscopy [91]. It is not considered trivial, however, to apply AFM to membranes under an aqueous layer. Here the evaluation of the fluidity was inferred indirectly from the single molecule traces. Despite the disadvantage of indirect evaluation, this method nonetheless allowed me to evaluate each sample used. Since membrane integrity may vary from sample to sample, constant control is important. A mean defect area fraction of 3.6 % was found for the model membranes used to test the NEP. Membranes with large, visible defects were excluded from the analysis. This minimized the effect of

defects on the determination of MFPT. The analysis cannot determine the cause of the defects. However, no further improvements to the membrane formation and substrate cleaning protocols are planned as the membrane quality achieved was found to be sufficient. In addition, lipids that come into contact with membrane defects adhere to them, become immobile, and bleach out. Therefore, these molecules do not appear in the MFPT analysis.

The particles of the mobile fraction were tested for free diffusion. The diffusion coefficient was also determined where appropriate. Free diffusion is an important prerequisite for an analysis of the mean first passage time. The diffusivity was confirmed by two different techniques: using the linear regime of the mean squared displacement over time, and the Gaussian distribution of the 1D step distributions. Both methods are commonly used, although the second is considered to be more robust. However, this only provides an averaged view which does not necessarily indicate variations in diffusion [94]. The quality of the linear fit was measured by the $R^2$ value of 0.98, which was very close to one, indicating free diffusion. Furthermore, the fit gave a diffusion coefficient of $D = 2.29 \pm 0.05 \mu m^2/s$, which is in agreement with results obtained from comparable model membranes imaged at room temperature [95, 96]. The diffusivity of the traced lipids in the model membrane patches was further confirmed by the demonstration of the normal distribution of the 1D step distributions by a Gaussian fit. The diffusive behavior was analyzed further after diffusivity was established in general.

The analysis of the 1D step distributions of the particle traces revealed two diffusive fractions aside from an immobile fraction. The traces were separated as described in Section 4.6.1 with an algorithm previously published in [97]. The fractions had distinct diffusion coefficients with the so-called slow fraction, $\sim 40\%$, moving at only $0.17 \pm 0.17\ \mu m^2/s$. This value differs by an order of magnitude from the diffusion coefficient of the so-called fast fraction, $\sim 60\%$, which moved at $2.67 \pm 0.13\ \mu m^2/s$. Both fractions include all lipid trajectories, regardless of whether the lipid tracer reached an exit site. The determination of $\tau$ from Equation 6 requires the contribution of particles starting at least from the center of the domain. The probability to travel the distance from at least the center to the escape site during the observation time was naturally lower for slow particles. As a result, none of the traces and trace parts categorized as slow contributed to the resulting $\tau$ in the MFPT analysis.

The diffusion coefficient of all fast lipids which did escape and were therefore used in the MFPT analysis was 2.29 ± 0.05 $\mu m^2/s$, this diffusion coefficient is further used in the theoretical and *in silico* determination of the MFPT. Traces from both categories were found to be equally distributed in the membrane patches. Studies with intracellular labels suggest that ATTO 647N can lower the average diffusion coefficient of the labeled protein [98]. Hughes demonstrated that, like many other fluorescent dyes, ATTO 647N has the potential to show a general association with PC lipid bilayers [99]. A hypothesis to investigate further would therefore be the interaction of the labeled lipids as a cause for slowed down diffusion. A change in the diffusive behavior could be a potential outcome, however. The interaction of labeled and unlabeled lipids as a cause seems unlikely at this point. Because of the great abundance of unlabeled lipids I would expect interaction and subsequent sub-diffusion to appear more frequently. It cannot be ruled out at this point, however. The presence of a slow and a fast diffusive fraction has already been observed by Schoch and co-researchers, who found evidence of a slow fraction in the lower leaflet and a corresponding fast fraction in the upper leaflet. In their case, the tracer molecule was DMPE, a PE lipid with a shorter tail (14 C atoms) than the DOPE (18 C atoms) used in my experiment, but labeled with the same ATTO647N dye. Furthermore, the SLBs were prepared in such a way that the tracer lipids initially occurred in both leaflets [100]. In the experiments described in this dissertation, the tracer lipids were added only to the upper leaflet. However, a relatively large slow fraction of tracer was reported. Therefore, it remains unclear whether flip-flop events would be frequent enough to cause the described tracer lipids to be transported to the lower leaflet. The reason for the existence of different diffusion fractions in the context of the model system presented in this study has not yet been conclusively investigated.

The $MSD/t$ analysis indicated an average free diffusion within the diffusion domains. To ensure unbiased diffusion, specifically at the rim of the domains, site-specific diffusion was analyzed from the one-step distributions of the traces. The separation of the rim and the center area was based on a compromise between maximal coverage of 1-step events and minimal inclusion of 2-step events. Comparing possible rim widths resulted in a reasonable threshold of 320 $nm$, equal to 2 pixels. Separation of the one-step and two-step events is another issue to consider. The

diffusion steps result from overlapping length distributions. Therefore, the fractions will not be clearly separable by length. A sub-pixelation technique may provide an improvement in the resolution of particle dynamics that is independent of the camera chip used. This hypothesis contrasts with the idea that the contribution of 2-step events to the trace data at the rim is likely to introduce the largest error. It would be beneficial to perform additional experiments to investigate whether a finer resolution would allow for a more accurate analysis of rim interactions. For the time being, however, the presented method seems to be sufficient. It might be possible to sort the traces with visible reflections by hand. There will, however, be a limited number of reflection events that can be resolved individually this way.

The locus-specific analysis of the 1D displacements revealed the free diffusion in the rim and center area. Further, the mobility at the rim was interesting to assess, because the traces analyzed here included the interaction events at the gold boundary. Reflection is not directly measured in our experimental setup. A limitation is imposed by the limited resolution of particle dynamics as a result of the imaging time lag. As an indirect inference of the trace parts involved in a reaction at the gold boundary, a rim area was defined. The chosen rim width reduces the bias from diffusion angles which were most likely not involved in a reflection event. The reflectivity was tested by evaluating the angles between consecutive steps of particle traces in the rim area. As stated in Harrison et al. [101], a tendency of consecutive angles towards $[90° > \theta < 270°]$ indicates tethered motion whereas overpopulated values in the range of $[90° < \theta < 270°]$ are a typical sign of directed motion. In this study, the angles calculated from data at the rim and in the center both showed an unbiased distribution, which is typical for Brownian motion [101]. It is critical to note that the resolution of the imaging method does not allow visualization of the reflection events in isolation. Nevertheless, reducing the rim width ensures that most step angles will include interaction with the rim. The even distribution of the angles in the rim and center area indicate an unbiased reflectivity. Although the directionality of the steps was not affected, a reduction in the diffusion coefficient from $D_{center} = 2.21 \pm 0.01\,\mu m^2/s$ to $D_{rim} = 1.13 \pm 0.02\,\mu m^2/s$ was observed. The elastic collision, in which the total kinetic energy of the collision partners is conserved during the collision process, is an idealization. In practice, the sum of the kinetic energies of the collision partners after the collision is always slightly less than

the sum of the kinetic energies before the collision. In these inelastic collisions the kinetic energy is transformed into internal energy [102]. In the case of lipids in a membrane, a change in the internal energy can be seen in the deformation of the volume or area they occupy in the membrane [103]. The reduction of the diffusion coefficient in the rim area can be seen as evidence of the reduction of kinetic energy inflicted on a particle's motion by a reflection event. Naturally, the general effect of the reflection on the particle dynamics grows with decreasing domain size. Due to this eventual bias, smaller domains are potentially not suitable as a model to the narrow escape problem. The localization precision of $\sigma_\gamma = 19\,nm$ in the patterned membranes of the described model system was found to be high in comparison to unpatterned supported lipid bilayers, where values around $30\,nm$ are common [23]. Accurate localization affects the possible size of the area and the density of particles observed, thus increasing throughput. Localization accuracy is an important factor to consider at the escape site because it can affect the mean first passage time, and inaccurate localization can introduce bias. Due to the margin of error defined by $\sigma$, particles may be counted as escaped before hitting the escape site, leading to an underestimation of escape times. Therefore, it is important to set the size of the escape site reasonably large in relation to the localization accuracy to get the most reliable results for the $\tau$.

## 4.2 The experimental test of the influence of $\varepsilon$ on $\tau$

Initial experimental results revealed that the mean first passage time stayed constant with changes in the escape opening size, $\varepsilon$. This result leads to the discovery of the strong effect of the photo-stability and therefore the lifetime limitation of the tracer lipids on the mean first passage time. As described in Section 1.5.3 ATTO647N was specifically chosen for its representative role. Even though the label is known for its photo-stability [34], it proved far from efficient on the timescales needed to capture the rare event of escape in the experimental setup. This limitation underlines the importance of a straightforward solution to the problem of photostability in the context of the narrow escape problem.

In the case of live-cell imaging, fluorescent dyes are of great importance and cannot be substituted by other labels like quantum dots, gold beads, or nanodiamonds in many applications. Thus, the limitations of fluorescent dyes need to be considered. Other possible fluorescent labels, as SeTau-647-NHS, [104] (quantum yield $\Phi = 0.61$, extinction coefficient $\epsilon_{max} = 200,000\ M^{-}1\ cm^{-}1$)[105] or Janelia Fluor-JF646 (quantum yield $\Phi = 0.54$, extinction coefficient $\epsilon_{max} = 152,000\ M^{-}1\ cm^{-}1$) [87], with enhanced brightness and photo-stability hold the prospect of reducing the limiting effects to a certain extent while still providing the advantages of a fluorescent dye. The latter will broaden the accessible range of $\bar{\tau}$, but not to an extent in which the correct measurement of mean first passage time would be in reach.

Further, a theoretical approach to determine $\bar{\tau}$ will be difficult since there are only analytical models for simple geometries so far [106]. However, specific biological applications such as those in the field of immunology or parasitology will have complex, unique diffusion domains in which specific geometrical parameters, essential for the determination of the MFPT, are not known. In this case, the experimental determination of $\bar{\tau}$ will be the only solution. A rare escape event may, however, be difficult to observe due to the sample properties and fluorophore limitations described earlier.

The theoretical research on the topic of Brownian particle mortality concerning the narrow escape problem [14, 107, 108, 109], as well as the complex mathematical extension to the theory by Grebenkov and Rupprecht, [106] do not provide a straightforward solution for the experimentalist. With the correction factor intro-

duced in this thesis this gap is closed. By this easy-to-apply method to re-scale the mean first passage time by the fraction of escaped particles, $\bar{\tau}$ can now be determined in applications where fluorescent dyes remain obligatory and were previously experimentally inaccessible. With the re-scaled *in vitro* experiments, I showed that the absolute mean first passage time and the logarithmic dependence on the escape opening are in agreement with the theoretical predictions in the limit of small escape openings. This favorable agreement allows me to conclude that the reduced diffusion coefficient at the rim had a negligible effect on $\tau_{exp,corr}$. For sufficiently large diffusion domains, this holds true. One should, however, consider adding additional passivization to the gold to prevent edge effects when using smaller membrane patches in future experiments [77].

From the literature, we know that that the mean first passage time is predominately defined by the area, escape site size of the diffusion domain and the diffusion coefficient of the tracer particle. Following the escape site size, the area of the domain and the diffusion coefficient should be the next parameters to fully test systematically. To this end, it will be possible to complement the existing experiments and simulations. The enlargement of the diffusion domain will, in both *in silico* and *in vitro* experiments, come with specific difficulties. Regarding the simulations, the processing of larger domains will lead to an increased demand for time and power, which can become a technical hurdle. The size of the *in vitro* diffusion domain can be defined by the use of colloids, which can be obtained commercially in any size. Nevertheless, the variation in the possible size of the diffusion domain is limited. The domains chosen should not be too small, to avoid energy loss during the reflection event becoming a predominant factor. On the other hand, the size is restricted by the traceability of the tracer particle, as especially large domains might not be sufficiently explored. The diffusion coefficient of the tracer lipids can be easily and directly varied by the temperature settings. The limits of this method lie in the phase behavior of the lipid matrix for lower diffusion coefficients and the possible acquisition frequency for higher diffusion coefficients. Another way to introduce variation in the diffusion coefficient is a changed lipid composition, which can have different effects depending on the type of used lipid or composition [26, 27, 28]. From the literature we know that the symmetry of the diffusion domain can also have a large influence on the mean first passage time [15]. Therefore, another interesting

step would be to investigate the mean first passage time in asymmetric diffusion domains by simulation in the future. However, the systematic test of the mean first passage time in asymmetric domains *in vitro* would require a different approach of a simplified but easy-to-control model system, not dependent on symmetrical colloids.

## 4.3 Random walk simulations to complement the experimental test of the narrow escape problem

Random walk simulations are known to be a versatile tool to study complex molecular dynamics [110, 111]. In this dissertation, I performed random walk simulations to complement the experimental exploration of various aspects of the narrow escape problem in the very simple setting of the disk. The simulations are a useful tool to support the experimental investigation as well as to explore aspects of the research question that are not accessible with the *in vitro* approach.

The simulation scenario was characterized with respect to independence of the chosen starting point of the diffusing particle as well as the necessary statistics to achieve $\tau$ reliably. Theoretical considerations of the effect of the starting points distance from the escape site predict an initial increase of $\tau$ followed by saturation at a distance one radius and larger [14]. In this dissertation, a set of simulations with increasing distances of the start loci from the escape site showed a strong dependence of $\tau$ on distance up to 60 % of the domain diameter. Full saturation was observed at 80 % of the diameter (Section 3.4.3). The influence of the size of the escape opening was not considered in the theory so far. The experiments of this thesis indicate, that there was no difference in the effect of escape opening sizes on $\tau$ for the escape opening sizes tested. It was also found that the starting locus, whether in the center of the domain or randomly distributed, had no effect on the mean first passage time. An experiment on the robustness of the determination of $\tau$ from escape time distributions suggested that at least 800 escape times are needed to ensure a reliable value, Section 3.4.2. This is particularly valuable for setting other results in relation to their statistical significance.

The observed deviation between simulation and theory regarding the independence of $\tau$ on the starting distance can be explained by insufficient statistics. No set of simulated traces achieved 800 representatives, typically 400 simulated particles escaped per starting distance. This seems especially likely since the evaluation of the starting locus with sufficient statistics did not show any dependence on the center and random starts further away from a on $\tau$. In the future these early simulations should be completed by additional representatives.

In the experiments testing the NEP problem, the simulations were set up accord-

ing to the characterization above. Particles started from the center of the domain and the number of particles were chosen sufficiently to always achieve statistics of well above 800. Furthermore, it was shown that the experimentally inspired *in silico* experiment closely mimics the *in vitro* experiment. With the good representation of the *in vitro* data, we now had the opportunity to use the *in silico* data to make a prediction about the experimental situation. On the other hand, the agreement is another piece of evidence that the particles in the membrane model do perform Brownian motion. With the presented *in silico* experiments, where $\tau_{sim,\infty}$ and $\tau_{sim,corr}$ agreed, it was possible to prove that the suggested re-scaling by the escaped fraction of particles is a valid method to correct for lifetime limitation in particle tracks. Both results, from simulations and corrected *in vitro* experiments, were in good agreement with the theoretical result for the mean first passage time. The diffusion simulations assume a simplified model of the system under investigation. For example, the model assumes that the diffusing particles are identical, that there are no barriers to diffusion within the diffusion domain, and that there are no interactions between the particles. While these assumptions facilitate the simulations, they can limit the accuracy of the results. In my case the results, $\tau_{sim}$, derived from this simplified model, match the experimental and theoretical results, however. The model is a powerful tool for testing hypotheses. In our specific case, computational hardware and time was an issue, making more complex applications inaccessible at this time. With an improved, more resourceful simulation design, in terms of speed, one should repeat the *in silico* experiments for a variation of the diffusion domain radius. The code developed in this thesis already offers this possibility, but it has not been pursued so far. Furthermore, different geometries could be tested. In general, it is possible to create very complex diffusion scaffolds with different escape domains to counter test or complement knowledge about dynamics in the biological context. A direct example of an application combining NEP and random walk simulations is the simulation of VSG dynamics described by Schwebs [41]. She showed that random walk is sufficient to facilitate the turnover of the variant surface glycoprotein (VSG) coat in African trypanosomes.

## 4.4 The astigmatism-based 3D single-molecule fluorescence microscopy extension

Astigmatism-based 3D single-molecule fluorescence microscopy (3D SMFM) derives information about the dynamics of a single molecule from an extended focal plane. With this method, dynamics can be resolved continuously from volumetric samples in *in vivo* without losing potentially critical time points while imaging stacks [58, 81]. The general concept of astigmatism-based 3D SMFM has been established for some time [58, 59, 81]. In our case, the method was particularly attractive because only a limited number of modifications are required to add a 3D extension to an existing wide-field single-molecule fluorescence microscope hardware. In addition, a variety of potential software solutions can be found in the literature [61].

The status of the successful hardware adaptation of a 3D extension to our single-molecule microscopy setup has been described in this thesis in Section 3.5. In the future, it is planned to complete the integration of a solution for the analysis of the 3D super-resolution data into our existing image processing pipeline. This will ensure maximum comparability with existing and future results.

As an adaptation, a piezo stepper was integrated under the objective. Additionally, a weak cylindrical lens with a focal length of $f = 1\,m$ was mounted in a C-mount to introduce astigmatism, as described in Section 3.5.1. While the piezo stepper is a relatively simple model, the smooth calibration curve of the beads indicates that a step resolution of $10\,nm$ is sufficient for my purpose. The range of the P-721.SL2 PIFOC was a maximum of $140\,\mu m$. I found a limitation in distinguishing PSF deformation in the range of 300 to 600 $nm$, and the optimal imaging depth to be expected with the lens used is $1\,\mu m$ [61], both well below the $140\,\mu m$ limit, proving that the P-721.SL2 PIFOC is a sufficient device for my application. The installation of a matching piezo controller allowed synchronization with the existing image management system controlled by the $\mu$-Manager software. This provided a streamlined and simple application. The image analysis pipeline was adapted to fit the existing algorithms, ensuring good comparability of future 3D tracking results to existing 2D results. For example with VSG dynamics, as published in [41]. The accuracy of the astigmatism calibration can have a significant impact on the accuracy of the z-position determination. The linear fit to the ellipticity was a first, straight-

forward attempt to generate a calibration curve. Experiments on the calibration curves revealed that the newly installed lens allowed a realistic working depth of about 300 $nm$ for samples with an ATTO647N label and about 600 $nm$ when the calibration curve was derived from multi-fluorescent beads, Section 3.5.1.3. This is in contrast to the optimal achievable depth of 1 $\mu m$ [61]. In general, it was seen that the calibration curves yielded more accurate values for signal positions closer to the glass cover-slip. This effect could be explained by the smaller influence of the refraction index mismatch when imaging closer to the glass. McGorty [85] demonstrated how to increase z accuracy by correcting for the aberration introduced by the refraction mismatch between an oil immersion objective and an aqueous sample. The correction resulted in an axial resolution throughout the depth of the sample of 50-60 $nm$ and a lateral resolution of 20-30 $nm$ in their example. After evaluating whether the refraction mismatch is indeed the cause of this observation, a correction could be attempted to increase the axial resolution in the calibration curve and thus the imaging depth in the experiment. To apply the correction it is necessary to determine the phase of the pupil function, which encodes the astigmatic deformation as well as all intrinsic aberrations of the imaging system [85, 112]. In addition to a series of example images of the PSF at different focal planes, the refractive index of the hydrogel and the optical path length are also relevant. However, a correction for the refraction mismatch was not successfully applied so far, as the method is not entirely trivial to apply and requires information that was not available at this point in the work. Besides the correction of the refraction mismatch, an additional improvement can be made with the fit of the calibration curve. Simply reducing the elliptical deformation to its linear part reduces the possible resolvable range in z. In addition, the fit itself is prone to errors. A more flexible approach uses a spline fit instead of a linear one. The spline fit provides a more sufficient image of the calibration curve beyond the linear or quadratic regime. This is achieved by placing multiple lower-order polynomials through the given data points so that a polynomial is defined between every two data points. The more accurate fit can increase the accessible imaging depth [80]. An accurate calibration curve is required to accurately determine the axial positions of individual molecules in the experiment. Initial experiments resulted in single molecule localizations with a lateral localization precision, $\sigma_{x,y}$, of 26 $nm$. This is in very good agreement with the reported

optimal resolution for a similar technique of $\sigma_{x,y}$, of 26-28 $nm$ [61]. The determined axial resolution, $\sigma_z$, of 120 $nm$ was found to be less good than the values of $\sigma_z$, of 29-66 $nm$ reported in the literature, however [61]. Limited axial accuracy prevents meaningful analysis of the imaged single particle dynamics. To advance this 3D SMFM approach, a variety of improvements need to be tested. As described in the introduction, increasing the number of photons collected in an observation time point can improve the accuracy of localization. This can generally be achieved by making changes to the microscopy setup, such as increasing the illumination power or exposure time, using a high quantum yield emitter, or using a brighter fluorescent label. One aspect not yet addressed in this work is processing the acquired 3D single-molecule data. The Super-Resolution Microscopy Analysis Platform (SMAP) is a tool that allows quick access to initial tracking and tracking analysis results through an all-in-one visualization interface [113]. The same is true for TrackIt [88]. Both tools can export the tracking data to Matlab files. However, it will be advantageous to add better immersion into existing image analysis pipelines and include comparability with past experiments in the group. To this end, the future goal is to complete the establishment of an adapted imaging pipeline for 3D SMFM data, building on software currently used in our group.

## 4.5 Concluding remarks

In this dissertation, I have systematically tested the mean first passage time as a function of the escape aperture $\varepsilon$ in a diffusion domain with the shape of a disk. For a comprehensive approach, I combined *in vitro* and *in silico* experiments. Both results were in excellent agreement with the theory. The newly established membrane model system for the *in vitro* experiments proved to be very suitable for the approach. The problem of lifetime limitation of the fluorescently labeled tracer lipids was successfully solved by the introduction of an easy-to-apply correction factor. This correction factor was validated by *in silico* experiments. Moreover, the membrane model system provides an opportunity to address the functional dependence of $\bar{\tau}$ on the remaining parameters $A$ and $D$ in future experiments. In a side project, I installed the necessary hardware for an astigmatism-based 3D single-molecule fluorescence microscope. So far, further evaluation is needed, especially to increase the axial localization precision of the single particles. Furthermore, the image analysis pipeline has to be established and tested for compatibility with existing software.

# Bibliography

[1] M Weiss. Crowding, diffusion, and biochemical reactions. International review of cell and molecular biology, 307:383–417, 2014.

[2] S F Fenz, A Pezzarossa, and T Schmidt. The Basics and Potential of Single-Molecule Tracking in Cellular Biophysics, Comprehensive Biophysics, volume 2. Oxford: Academic Press, 2012.

[3] A Einstein. Über die von der molekularkinetischen Theorie der Wärme geforderte Bewegung von in ruhenden Flüssigkeiten suspendierten Teilchen. Annalen der Physik, 4, 1905.

[4] D Ernst and J Köhler. How the number of fitting points for the slope of the mean-square displacement influences the experimentally determined particle size distribution from single-particle tracking. Physical Chemistry Chemical Physics, 15(10):3429–3432, 2013.

[5] T Lagache and D Holcman. Extended narrow escape with many windows for analyzing viral entry into the cell nucleus. Journal of Statistical Physics, 166(2):244–266, 2017.

[6] D S Grebenkov, D Holcman, and R Metzler. Preface: new trends in first-passage methods and applications in the life sciences and engineering. Journal of Physics A: Mathematical and Theoretical, 53(19):190301, 2020.

[7] D Holcman and Z Schuss. Escape through a small opening: receptor trafficking in a synaptic membrane. Journal of Statistical Physics, 117(5):975–1014, 2004.

[8] A Singer, Z Schuss, and D Holcman. Narrow escape, Part II: The circular disk. Journal of statistical physics, 122(3):465–489, 2006.

[9] Z Schuss, A Singer, and D Holcman. The narrow escape problem for diffusion in cellular microdomains. Proceedings of the National Academy of Sciences, 104(41):16098–16103, 2007.

[10] S Pillay, M J Ward, A Peirce, and T Kolokolnikov. An asymptotic analysis of the mean first passage time for narrow escape problems: Part I: Two-dimensional domains. Multiscale Modeling & Simulation, 8(3):803–835, 2010.

[11] A F Cheviakov, M J Ward, and R Straube. An asymptotic analysis of the mean first passage time for narrow escape problems: Part II: The sphere. Multiscale Modeling & Simulation, 8(3):836–870, 2010.

[12] J S Marshall. Analytical solutions for an escape problem in a disc with an arbitrary distribution of exit holes along its boundary. Journal of Statistical Physics, 165(5):920–952, 2016.

[13] J Reingruber, E Abad, and D Holcman. Narrow escape time to a structured target located on the boundary of a microdomain. The Journal of chemical physics, 130(9):094909, 2009.

[14] D Holcman and Z Schuss. Stochastic narrow escape in molecular and cellular biology. Analysis and Applications. Springer, New York, 48:108–112, 2015.

[15] F Wei, D Yang, R Straube, and J Shuai. Brownian diffusion of ion channels in different membrane patch geometries. Physical Review E, 83(2):021919, 2011.

[16] D Holcman and Z Schuss. Control of flux by narrow passages and hidden targets in cellular biology. Reports on Progress in Physics, 76(7):074601, 2013.

[17] Y M Chan and S G Boxer. Model membrane systems and their applications. Current opinion in chemical biology, 11(6):581–587, 2007.

[18] D Bach and E Wachtel. Phospholipid/cholesterol model membranes: formation of cholesterol crystallites. Biochimica et Biophysica Acta (BBA)-Biomembranes, 1610(2):187–197, 2003.

[19] N F Morales-Penningston, J Wu, E R Farkas, S L Goh, T M Konyakhina, J Y Zheng, W W Webb, and G W Feigenson. GUV preparation and imaging: minimizing artifacts. Biochimica et Biophysica Acta (BBA)-Biomembranes, 1798(7):1324–1332, 2010.

[20] K B Blodgett. Films built by depositing successive monomolecular layers on a solid surface. Journal of the American Chemical Society, 57(6):1007–1022, 1935.

[21] I Langmuir, V J Schaefer, and H Sobotka. Multilayers of sterols and the adsorption of digitonin by deposited monolayers. Journal of the American Chemical Society, 59(9):1751–1759, 1937.

[22] S J Singer and G L Nicolson. The fluid mosaic model of the structure of cell membranes: Cell membranes are viewed as two-dimensional solutions of oriented globular proteins and lipids. Science, 175(4023):720–731, 1972.

[23] T Schmidt, G J Schütz, W Baumgartner, H J Gruber, and H Schindler. Imaging of single molecule diffusion. Proceedings of the National Academy of Sciences, 93(7):2926–2929, 1996.

[24] S Mayor and M Rao. Rafts: scale-dependent, active lipid organization at the cell surface. Traffic, 5(4):231–240, 2004.

[25] G W Feigenson. Phase diagrams and lipid domains in multicomponent lipid bilayer mixtures. Biochimica et Biophysica Acta (BBA)-Biomembranes, 1788(1):47–52, 2009.

[26] M Edidin. The state of lipid rafts: from model membranes to cells. Annual review of biophysics and biomolecular structure, 32(1):257–283, 2003.

[27] D Krapf. Mechanisms underlying anomalous diffusion in the plasma membrane. Current topics in membranes, 75:167–207, 2015.

[28] N Destainville, F Dumas, and L Salomé. What do diffusion measurements tell us about membrane compartmentalisation? Emergence of the role of interprotein interactions. Journal of chemical biology, 1(1):37–48, 2008.

[29] J Song and R E Waugh. Bending rigidity of SOPC membranes containing cholesterol. Biophysical Journal, 64(6):1967–1970, 1993.

[30] P Pomorski, S Hrafnsdóttir, P F Devaux, and G van Meer. Lipid distribution and transport across cellular membranes. Seminars in Cell & Developmental Biology, 12(2):139–148, 2001.

[31] F Heinemann and P Schwille. Preparation of Micrometer-Sized Free-Standing Membranes. ChemPhysChem, 12(14):2568–2571, 2011.

[32] J T Groves, N Ulman, and S G Boxer. Micropatterning fluid lipid bilayers on solid supports. Science, 275(5300):651–653, 1997.

[33] C K Yee, M L Amweg, and A N Parikh. Direct photochemical patterning and refunctionalization of supported phospholipid bilayers. Journal of the American Chemical Society, 126(43):13962–13972, 2004.

[34] O Shimomura, F H Johnson, and Y Saiga. Extraction, purification and properties of aequorin, a bioluminescent protein from the luminous hydromedusan, aequorea. Journal of Cellular and Comparative Physiology, 59(3):223–239, 1962.

[35] A M Alkilany, S E Lohse, and C J Murphy. The gold standard: gold nanoparticle libraries to understand the nano–bio interface. Accounts of chemical research, 46(3):650–661, 2013.

[36] K Bley, J Semmler, M Rey, C Zhao, N Martic, T Klupp, N Robin, M Stingl, and N Vogel. Hierarchical design of metal micro/nanohole array films optimizes transparency and haze factor. Advanced Functional Materials, 28(13):1706965, 2018.

[37] B D Almquist and N A Melosh. Fusion of biomimetic stealth probes into lipid bilayer cores. Proceedings of the National Academy of Sciences, 107(13):5815–5820, 2010.

[38] E Abbe. Beiträge zur Theorie des Mikroskops und der mikroskopischen Wahrnehmung. Arch. Microsc. Anat, 9.1:413–468, 1873.

[39] J W 3rd Baron Rayleigh Strutt. On the theory of optical images, with special reference to the microscope. Journal of the Royal Microscopical Society, 23(4):474–482, 1903.

[40] Z Liu, L D Lavis, and E Betzig. Imaging live-cell dynamics and structure at the single-molecule level. Molecular cell, 58(4):644–659, 2015.

[41] M Schwebs. Structure and dynamics of the plasma membrane: a single-molecule study in Trypanosoma brucei. Ph.d. thesis, 02 2022.

[42] C E Hall. Introduction to electron microscopy, volume 77. LWW, 1954.

[43] R M Glaeser. Limitations to significant information in biological electron microscopy as a result of radiation damage. Journal of ultrastructure research, 36(3-4):466–482, 1971.

[44] F Kulzer and M Orrit. Single-molecule optics. Annu. Rev. Phys. Chem., 55:585–611, 2004.

[45] M Orrit and J Bernard. Single pentacene molecules detected by fluorescence excitation in a p-terphenyl crystal. Physical review letters, 65(21):2716, 1990.

[46] R M Dickson, A B Cubitt, R Y Tsien, and W E Moerner. On/off blinking and switching behaviour of single molecules of green fluorescent protein. Nature, 388(6640):355–358, 1997.

[47] N Bobroff. Position measurement with a resolution and noise-limited instrument. Review of Scientific Instruments, 57(6):1152–1157, 1986.

[48] M Lelek, M T Gyparaki, G Beliu, F Schueder, J Griffié, S Manley, R Jungmann, M Sauer, M Lakadamyali, and C Zimmer. Single-molecule localization microscopy. Nature Reviews Methods Primers, 1(1):1–27, 2021.

[49] R J Ober, S Ram, and E S Ward. Localization accuracy in single-molecule microscopy. Biophysical journal, 86(2):1185–1200, 2004.

[50] M S Robbins. Electron-multiplying charge coupled devices-emccds. Single-Photon Imaging, pages 103–121, 2011.

[51] JE Aubin. Autofluorescence of viable cultured mammalian cells. Journal of Histochemistry & Cytochemistry, 27(1):36–43, 1979.

[52] R E Thompson, D R Larson, and W W Webb. Precise nanometer localization analysis for individual fluorescent probes. Biophysical journal, 82(5):2775–2783, 2002.

[53] M Speidel, A Jonáš, and E-L Florin. Three-dimensional tracking of fluorescent nanoparticles with subnanometer precision by use of off-focus imaging. Optics letters, 28(2):69–71, 2003.

[54] P Prabhat, S Ram, E S Ward, and R J Ober. Simultaneous imaging of different focal planes in fluorescence microscopy for the study of cellular dynamics in three dimensions. IEEE transactions on nanobioscience, 3(4):237–242, 2004.

[55] M F Juette, T J Gould, M D Lessard, M J Mlodzianoski, B S Nagpure, B T Bennett, S T Hess, and J Bewersdorf. Three-dimensional sub-100 nm resolution fluorescence microscopy of thick samples. Nature methods, 5(6):527–529, 2008.

[56] S R P Pavani and R Piestun. Three dimensional tracking of fluorescent microparticles using a photon-limited double-helix response system. Optics express, 16(26):22048–22057, 2008.

[57] S R P Pavani, M A Thompson, J S Biteen, S J Lord, N Liu, R J Twieg, R Piestun, and W E Moerner. Three-dimensional, single-molecule fluorescence imaging beyond the diffraction limit by using a double-helix point spread function. Proceedings of the National Academy of Sciences, 106(9):2995–2999, 2009.

[58] H P Kao and A S Verkman. Tracking of single fluorescent particles in three dimensions: use of cylindrical optics to encode particle position. Biophysical journal, 67(3):1291–1300, 1994.

[59] L Holtzer, T Meckel, and T Schmidt. Nanometric three-dimensional tracking of individual quantum dots in cells. Applied Physics Letters, 90(5):053902, 2007.

[60] B Huang, W Wang, M Bates, and X Zhuang. Three-dimensional super-resolution imaging by stochastic optical reconstruction microscopy. Science, 319(5864):810–813, 2008.

[61] D Sage, T Pham, H Babcock, T Lukes, T Pengo, J Chao, R Velmurugan, A Herbert, A Agrawal, S Colabrese, et al. Super-resolution fight club: assessment of 2D and 3D single-molecule localization microscopy software. Nature methods, 16(5):387–395, 2019.

[62] R Lévy, U Shaheen, Y Cesbron, and V Sée. Gold nanoparticles delivery in mammalian live cells: a critical review. Nano Reviews, 1(1):4889, 2010. PMID: 22110850.

[63] L P Suarez-Kelly, S H Sun, C Ren, I V Rampersaud, D Albertson, M C Duggan, T C Noel, N Courtney, N J Buteyn, C Moritz, et al. Antibody conjugation of fluorescent nanodiamonds for targeted innate immune cell activation. ACS applied nano materials, 4(3):3122–3139, 2021.

[64] S Garifo, D Stanicki, G Ayata, R N Muller, and S Laurent. Nanodiamonds as nanomaterial for biomedical field. Frontiers of Materials Science, pages 1–18, 2021.

[65] P P Mathai, J A Liddle, and S M Stavis. Optical tracking of nanoscale particles in microscale environments. Applied Physics Reviews, 3(1):011105, 2016.

[66] K Murase, T Fujiwara, Y Umemura, K Suzuki, R Iino, H Yamashita, M Saito, H Murakoshi, K Ritchie, and A Kusumi. Ultrafine membrane compartments for molecular diffusion as revealed by single molecule techniques. Biophysical Journal, 86(6):4075–4093, 2004.

[67] A Gemeinhardt, M P McDonald, K König, M Aigner, A Mackensen, and V Sandoghdar. Label-free imaging of single proteins secreted from living cells via iSCAT microscopy. JoVE (Journal of Visualized Experiments), .(141):e58486, 2018.

[68] R Yuste. Fluorescence microscopy today. Nature methods, 2(12):902–904, 2005.

[69] J Lippincott-Schwartz and G H Patterson. Development and use of fluorescent protein markers in living cells. science, 300(5616):87–91, 2003.

[70] D M Chudakov, S Lukyanov, and K A Lukyanov. Tracking intracellular protein movements using photoswitchable fluorescent proteins PS-CFP2 and Dendra2. Nature protocols, 2(8):2024–2032, 2007.

[71] R Ando, H Hama, M Yamamoto-Hino, H Mizuno, and A Miyawaki. An optical marker based on the UV-induced green-to-red photoconversion of a fluorescent protein. Proceedings of the National Academy of Sciences, 99(20):12651–12656, 2002.

[72] E L Snapp. Fluorescent proteins: a cell biologist's user guide. Trends in Cell Biology, 19(11):649–655, 2009. Special Issue – Imaging Cell Biology.

[73] A C Croce and G Bottiroli. Autofluorescence spectroscopy and imaging: a tool for biomedical research and diagnosis. European journal of histochemistry: EJH, 58(4), 2014.

[74] M P Clausen and C B Lagerholm. The probe rules in single particle tracking. Current Protein and Peptide Science, 12(8):699–713, 2011.

[75] A Edelstein, N Amodaj, K Hoover, R Vale, and N Stuurman. Computer control of microscopes using $\mu$manager. Current protocols in molecular biology, 92(1):14–20, 2010.

[76] M W Davis and E M Jorgensen. ApE, a plasmid editor: a freely available DNA manipulation and visualization program. Frontiers in Bioinformatics, 2:818619, 2022.

[77] E Meiser, R Mohammadi, N Vogel, D Holcman, and S F Fenz. Experiments in micro-patterned model membranes support the narrow escape theory. bioRxiv, 2023.

[78] J M Smaby, J M Muderhwa, and H L Brockman. Is lateral phase separation required for fatty acid to stimulate lipases in a phosphatidylcholine interface? Biochemistry, 33(7):1915–1922, 1994.

[79] Marius G. Single-molecule fluorescence microscopy in live Trypanosoma brucei and model membranes. PhD thesis, University of Wuerzburg, 2018.

[80] S Proppert, S Wolter, T Holm, T Klein, S van de Linde, and M Sauer. Cubic B-spline calibration for 3D super-resolution measurements using astigmatic imaging. Optics express, 22(9):10304–10316, 2014.

[81] B Huang, S A Jones, B Brandenburg, and X Zhuang. Whole-cell 3D STORM reveals interactions between cellular structures with nanometer-scale resolution. Nature methods, 5(12):1047–1052, 2008.

[82] J S Hovis and S G Boxer. Patterning barriers to lateral diffusion in supported lipid bilayer membranes by blotting and stamping. Langmuir, 16(3):894–897, 2000.

[83] NATIONAL INSTITUTE OF STANDARDS and TECHNOLOGY/SEMATECH. e-handbook of statistical methods, 2013.

[84] W B Nelson. Applied life data analysis, volume 521. John Wiley & Sons, 2003.

[85] R McGorty, J Schnitzbauer, W Zhang, and B Huang. Correction of depth-dependent aberrations in 3D single-molecule localization and super-resolution microscopy. Optics letters, 39(2):275–278, 2014.

[86] D Spitznagel, J F O'Rourke, N Leddy, O Hanrahan, and D P Nolan. Identification and characterization of an unusual class i myosin involved in vesicle traffic in trypanosoma brucei. PloS one, 5(8):e12282, 2010.

[87] J B Grimm, T A Brown, B P English, T Lionnet, and L D Lavis. Synthesis of Janelia Fluor HaloTag and SNAP-tag ligands and their use in cellular imaging experiments. In Super-Resolution Microscopy, pages 179–188. Springer, 2017.

[88] T Kuhn, J Hettich, R Davtyan, and J C M Gebhardt. Single molecule tracking and analysis framework including theory-predicted parameter settings. Scientific reports, 11(1):1–12, 2021.

[89] E Dulkeith, M Ringler, TA Klar, J Feldmann, A Munoz Javier, and WJ Parak. Gold nanoparticles quench fluorescence by phase induced radiative rate suppression. Nano letters, 5(4):585–589, 2005.

[90] G P Acuna, M Bucher, I H Stein, C Steinhauer, A Kuzyk, P Holzmeister, R Schreiber, A Moroz, F D Stefani, T Liedl, et al. Distance dependence of single-fluorophore quenching by gold nanoparticles studied on DNA origami. ACS nano, 6(4):3189–3195, 2012.

[91] R P Richter, R Bérat, and A R Brisson. Formation of solid-supported lipid bilayers: an integrated view. Langmuir, 22(8):3497–3505, 2006.

[92] L K Tamm and H M McConnell. Supported phospholipid bilayers. Biophysical journal, 47(1):105–113, 1985.

[93] J Rädler, H Strey, and E Sackmann. Phenomenology and kinetics of lipid bilayer spreading on hydrophilic surfaces. Langmuir, 11(11):4539–4548, 1995.

[94] X Michalet. Mean square displacement analysis of single-particle trajectories with localization error: Brownian motion in an isotropic medium. Physical Review E, 82(4):041914, 2010.

[95] M Rose, N Hirmiz, J M Moran-Mirabal, and C Fradin. Lipid diffusion in supported lipid bilayers: a comparison between line-scanning fluorescence correlation spectroscopy and single-particle tracking. Membranes, 5(4):702–721, 2015.

[96] S F Fenz, R Merkel, and K Sengupta. Diffusion and intermembrane distance: case study of avidin and E-cadherin mediated adhesion. Langmuir, 25(2):1074–1085, 2009.

[97] T Bartossek, N G Jones, C Schäfer, M Cvitković, M Glogger, H R Mott, J Kuper, M Brennich, M Carrington, A Smith, et al. Structural basis for the shielding function of the dynamic trypanosome variant surface glycoprotein coat. Nature microbiology, 2(11):1523–1532, 2017.

[98] L C Zanetti-Domingues, C J Tynan, l J Rolfe, D T Clarke, and M Martin-Fernandez. Hydrophobic fluorescent probes introduce artifacts into single molecule tracking experiments due to non-specific binding. PloS one, 8(9):e74200, 2013.

[99] L D Hughes, R J Rawle, and S G Boxer. Choose your label wisely: water-soluble fluorophores often interact with lipid bilayers. PloS one, 9(2):e87649, 2014.

[100] R L Schoch, I Barel, F L H Brown, and G Haran. Lipid diffusion in the distal and proximal leaflets of supported lipid bilayer membranes studied by single particle tracking. The Journal of Chemical Physics, 148(12):123333, 2018.

[101] A W Harrison, D A Kenwright, T A Waigh, P G Woodman, and V J Allan. Modes of correlated angular motion in live cells across three distinct time scales. Physical biology, 10(3):036002, 2013.

[102] D Halliday, R Resnick, and J Walker. Fundamentals of physics. John Wiley & Sons, 2013.

[103] T Heimburg. Mechanical aspects of membrane thermodynamics. Estimation of the mechanical properties of lipid membranes close to the chain melting transition from calorimetry. Biochimica et Biophysica Acta (BBA) - Biomembranes, 1415(1):147–162, 1998.

[104] L Patsenker, A Tatarets, O Kolosova, O Obukhova, Y Povrozin, I Fedyunyayeva, I Yermolenko, and E Terpetschnig. Fluorescent probes and labels for biomedical applications. Annals of the New York Academy of Sciences, 1130(1):179, 2008.

[105] Y O Kudriavtseva, I G Yermolenko, O P Klochko, Y A Povrozin, E A Terpetschnig, and L D Patsenker. Setau dyes next generation long-wavelength biomedical labels with advanced characteristics.

[106] D S Grebenkov and J-F Rupprecht. The escape problem for mortal walkers. The Journal of chemical physics, 146(8):084106, 2017.

[107] D Holcman, A Marchewka, and Z Schuss. Survival probability of diffusion with trapping in cellular neurobiology. Physical Review E, 72(3):031910, 2005.

[108] D Holcman. Modeling DNA and virus trafficking in the cell cytoplasm. Journal of Statistical Physics, 127(3):471–494, 2007.

[109] B Meerson and S Redner. Mortality, redundancy, and diversity in stochastic search. Physical review letters, 114(19):198101, 2015.

[110] M Vogel and E Rössler. Effects of various types of molecular dynamics on 1D and 2D 2H NMR studied by random walk simulations. Journal of Magnetic Resonance, 147(1):43–58, 2000.

[111] K Huang and R J White. Random walk on a leash: a simple single-molecule diffusion model for surface-tethered redox molecules with flexible linkers. Journal of the American Chemical Society, 135(34):12808–12817, 2013.

[112] B M Hanser, M G L Gustafsson, D A Agard, and J W Sedat. Phase-retrieved pupil functions in wide-field fluorescence microscopy. Journal of microscopy, 216(1):32–48, 2004.

[113] J Ries. SMAP: a modular super-resolution microscopy analysis platform for SMLM data. Nature Methods, 17(9):870–872, 2020.

[114] M Carrington, N Miller, M Blum, I Roditi, D Wiley, and M Turner. Variant specific glycoprotein of Trypanosoma brucei consists of two domains each having an independently conserved pattern of cysteine residues. Journal of molecular biology, 221(3):823–835, 1991.

# List of Figures

# List of Tables

# Acknowledgements

Here I would like to thank all the people who have supported me during the journey of this dissertation. I feel very fortunate to have had supportive people around me to cover the various challenges of a Ph.D. thesis.

First of all, I would like to thank the Department of Cell and Developmental Biology with Markus Engstler as head of a very diverse and welcoming working environment. It was a great feeling to be at work and to experience scientific exchange in many meetings and seminars, as well as personal conversations and great friendships. I would especially like to thank Markus for his positive feedback and interest in my project during all our meetings.

I am grateful to Markus Sauer and Christian Stigloher for their valuable advice as thesis committee members.

I appreciated the scientific exchange with David Holcman, who is a real inspiration in the field of the narrow escape problem. Especially the ideas on the mathematical solution of the correction factor were of great help.

I am very thankful for the collaboration with Nicolas Vogel and Reza Mohammadi, through which I was able to generate the scaffolds for the pattered membrane model.

I would like to thank Brooke Morriswood for many inspiring conversations in the office and especially for his help with proofreading.

Susanne was the greatest inspiration of all, she lit the flame for biophysics and provided extraordinary personal and scientific support and guidance throughout our time together in the lab and afterwards.

A big thank you to all my friends, who always had my back through the ups and downs and made sure that the next upside was always in sight. You were always by my side for personal and scientific problems.

Finally, my amazing family. My parents and siblings, who helped me become who I am and never stopped believing in me, gently pushing me while providing a firm foundation.

# Appendix

## 4.6 Supplementary information

### 4.6.1 Separation of slow and fast diffusing fractions

In the analysis of the particle traces of the tracer lipids, a fraction of slower particles was noticed. The so-called slow fraction was separated from the fast fraction following the method described in [97]. The diffusion coefficients of both fractions were determined from the Gaussian fit to the 1D displacements and were found to be 2.67 $\pm$ 0.13 $\mu m^2/s$ and 0.17 $\pm$ 0.17 $\mu m^2/s$ for the fast and slow fraction, respectively. The function to separate the fractions is working with stretches of traces and not necessarily full traces. The determination of a precise fraction of full traces is not given, since a single trace can be cut in several fractions and several traces can be fused to a single stretch. Nevertheless, the number of localizations in both fractions gives a good estimate of the size of the two fractions. In this case, from a total of 563389 localizations, 337761 were categorized fast and 225628 slow. This roughly corresponds to $\sim$ 60% fast and $\sim$ 40% slow traces. Figure 27 gives an exemplary overview of the two fractions for one of the diffusion domains.

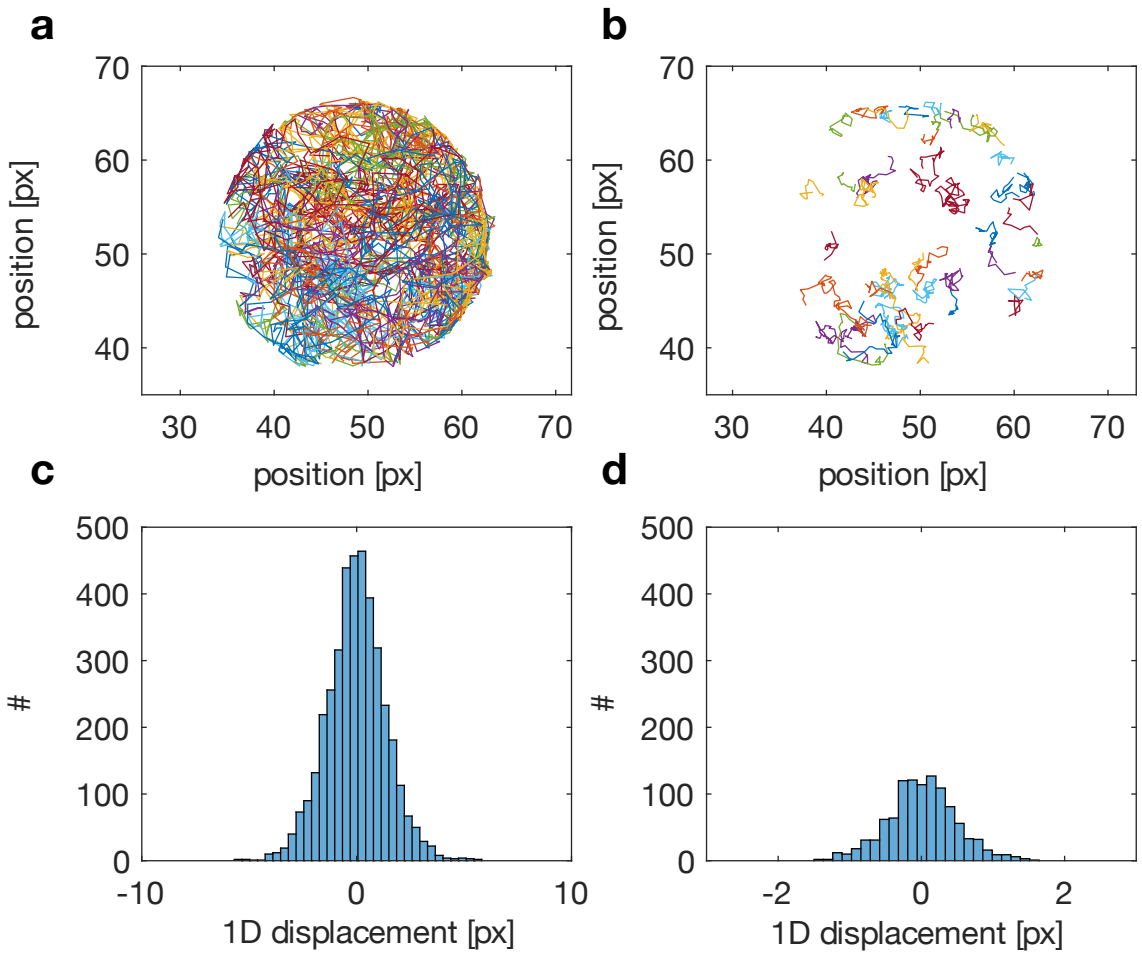


Figure 27: **Separation of slow and fast traces according to the diffusion coefficient of the particle. a,b** Plot of all single molecule traces categorized as fast and slow in one exemplary diffusion domain, respectively. **c,d** 1D displacement histograms illustrating the distribution of 1D diffusion step length of the tracer lipids categorized as fast and slow, respectively. The diffusion coefficients were derived a fit to the 1D displacements and are 2.67 $\pm$ 0.13 $\mu m^2/s$ and 0.17 $\pm$ 0.17 $\mu m^2/s$ for the fast and slow fraction, respectively.

### 4.6.2 Overview of all simulation parameters *

The full representation of all explicit values for $\tau$ from experiments, simulations and theory in Table 10 was as stated presented in [77].

Table 10: **Overview of simulation parameters and all explicit values for $\tau$ from experiments, simulations and theory.** From left to right: relative escape opening, temporal resolution in the simulation $\delta t[ms]$, ratio $\bar{l}/a[\%]$ of the mean step length $\bar{l}$ in simulations, and the window size a, $\bar{\tau}_{sim,\infty}$ from simulations with infinite particle lifetime, $\bar{\tau}_{sim,corr}$ from simulations with lifetime limited particles, the uncorrected measured mean first passage time $\bar{\tau}_{exp}$, the theoretical mean first passage time $\tau_{th}$, the lifetime corrected $\bar{\tau}_{exp,corr}$ and $p_{exp}$, which is the correction factor for the experimental data. Values marked with an asterisk are from simulations using a localization precision of $\sigma = 0$. All $\bar{\tau}$ are in $[s]$.

| $\varepsilon$ | $\delta t[ms]$ | $\bar{l}/a[\%]$ | $\bar{\tau}_{sim,\infty}$ | $\bar{\tau}_{sim,corr}$ | $\bar{\tau}_{exp}$ | $\tau_{th}$ | $\bar{\tau}_{exp,corr}$ | $p_{exp}$ |
|---|---|---|---|---|---|---|---|---|
| 1/8 | 10 | 16 | 5.66 | 4.68 | 0.411 | 7.90 | 4.86 | 0.084 |
| 1/12 | 10 | 23 | 7.12 | 6.17 | 0.432 | 8.96 | 6.54 | 0.066 |
| 1/16 | 10 | 31 | 8.40 | 8.19 | 0.435 | 9.72 | 7.69 | 0.057 |
| 1/20 | 10 | 39 | 9.15 | 9.85 | 0.438 | 10.30 | 8.68 | 0.050 |
| 1/24 | 10 | 47 | 9.87 | 9.96 | 0.455 | 10.78 | 9.75 | 0.047 |
| 1/32 | 10 | 63 | 12.00 | 12.05 | 0.464 | 11.53 | 11.15 | 0.042 |
| 1/44 | 5 | 60 | 11.49 | 11.86 | 0.464 | 12.36 | 12.37 | 0.038 |
| 1/56 | 4 | 70 | 12.94 | 13.33 | 0.466 | 12.99 | 13.31 | 0.035 |
| 1/72 | 2 | 65 | 13.78*,12.73 | 13.06 | 0.435 | 13.65 | 13.42 | 0.032 |
| 1/88 | 1.5 | 69 | 14.26*,12.88 | 13.15 | 0.434 | 14.17 | 14.18 | 0.031 |

## 4.7 Supplementary Materials for the cell line establishment

Table 11: ***T.brucei* cell lines.**

| Cell line | Description | Selection |
|---|---|---|
| MITat 1.6/ Lister 427 | Wild-type strain, Carrington et al. [114] | - |
| HaloTag::Myo1 | MITat 1.6 with the 3xTy1-Halo::TbMyo1 | blasticidin |

Table 12: ***T.brucei*** **cultivation and transfection.**

| Item | Components |
|---|---|
| HMI-9 medium | 176.6 g IMDM (Iscove's Dulbeccoo's Medium) |
| | 30.24 g NaHCO3 |
| | 143 $\mu l$ beta-mercaptoethanol |
| | 100 $ml$ penicillin/streptomycin |
| | 282 $mg$ bathocuproine sulfonate |
| | 390 $mg$ thymidine |
| | 1.36 $g$ hypoxanthine |
| | 1.82 $g$ L-cystine |
| | 10 % (v/v) FCS |
| | in 10 L $ddH_2O$, pH 7.5 |
| PBS | 10 $mM$ $Na_2HPO_4$ |
| | 1.8 $mM$ $KH_2PO_4$ |
| | 140 $mM$ $NaCl$ |
| | 2.7 $mM$ $KCl$ |
| | in 1 L $ddH_2O$, pH 7.4 |
| vPBS | 1x PBS |
| | 10 $mM$ glucose |
| | 46 $mM$ sucrose |
| TDB | 5 $mM$ $KCl$ |
| | 80 $mM$ $NaCl$ |
| | 1 $mM$ $MgSO_4$ |
| | 20 $mM$ $Na_2HPO_4$ |
| | 2 $mM$ $NaH_2PO_4$ |
| | 20 $mM$ glucose |
| | in 1 L $ddH_2O$, pH 7.7 |
| Nucleofector buffer | Lonza (CH) |
| Electroporation cuvettes | Amaxa (USA) |

## 4.8 Publication

Parts of this thesis are included in the following publication:

Elisabeth Meiser, Reza Mohammadi, Nicolas Vogel, David Holcman, and Susanne F. Fenz. Experiments in micro-patterned model membranes support the narrow escape theory. bioRxiv, 2023.